ABSTRACT

Title of dissertation: Chip-based photonic sensors for metrology and applications

Haitan Xu, Doctor of Philosophy, 2014

Dissertation directed by: Dr. Jacob Taylor and Dr. John Lawall
JQI, University of Maryland

Photonic sensors are of crucial importance in modern science and technology. They can be designed to be ultra-sensitive to certain physical quantities, while robust against other physical parameters. Many photonic sensors are compatible with CMOS technology and can be integrated on chips for use as highly sensitive, small scale and low cost sensors, such as ring resonator, disk resonator, Mach-Zehnder interferometer, photonic crystal, directional coupler, grating, etc. In this thesis we focus on two types of photonic sensors, micro-ring resonator and high contrast grating membrane, including their fabrication, theoretical basis, experimental characterizations, and their applications to the measurement of two fundamental physical quantities: temperature and length. We study chip-based micro-ring resonators, and show that ring resonator temperature sensors can be used to detect temperature differences as small as 80 μK, a 13-fold improved on previously reported results. We study a mirror-in-the-middle system with a high-reflectivity sub-wavelength grating. We show how the mode structure rapidly changes near the points where the left cavity and the right cavity simultaneously come into resonance, and suggest that

this is best understood via a perturbation theory starting from unit reflectivity, in contrast to the usual dispersive regime for membrane-in-the-middle work. In addition, the spectral signatures of the system allow more detailed study of the losses than is possible in a simple cavity, and we quantify the reflection, transmission, absorption and scattering losses in the context of a simple model. We use the mirror-in-the-middle system as a platform for high resolution absolute displacement measurement. This technique is based on radio frequency measurement without an optical reference. We have achieved a resolution of 4×10^{-14} m at a sampling rate of 10 Hz. This displacement sensing is used to analyze the stability and slow movement of the grating membrane in the mirror-in-the-middle cavity system. We also study theoretically two types of buckling transitions due to the optomechanical interaction between light and a grating membrane, which can be observed using our displacement sensing technique.

Chip-based photonic sensors for metrology and applications

by

Haitan Xu

Dissertation submitted to the Faculty of the Graduate School of the
University of Maryland, College Park in partial fulfillment
of the requirements for the degree of
Doctor of Philosophy
2014

Advisory Committee:
Professor Luis Orozco, Chair/Advisor
Professor Jacob Taylor, Advisor
Professor John Lawall, Advisor
Professor Steven Rolston, JQI Co-Director
Professor Edo Waks, Dean's representative

Dedication

To Qiuzi, Amelia and my parents

Acknowledgments

First I would like to thank my advisor, Dr. Jacob Taylor, for his strong support and guidance during the past more than five years. He can always give me inspring and helpful suggestions to my various research projects. It is a high honor to be one of his first students.

I would like to express my sincere appreciation to my co-advisor Dr. John Lawall, who kindly supported and guided me in my current experimental research on grating membrane and optomechanics. I also would like to thank Dr. Utku Kemiktarak, a member of both Drs. Taylor and Lawall's groups, from whom I have learnt various experimental skills. I enjoyed the time most when we overcame challenges together.

I acknowledge my collaborators in another project, including Drs. Alan Migdall, Jingyun Fan, Greg Strouse, Mohammad Hafezi, and Zeeshan Ahmed for their help and support throughout the thermal sensor project.

I am very thankful to Drs. Peter Zoller and Michael Levin for their very helpful and enlightening discussions in my research on topological physics.

I appreciate my former advisor, Dr. Xin Wan, who is always there encouraging me in my academic life.

I owe my gratitude to the staff at National Institute of Standards and Technology, including Kartik Srinivasan, Marcelo Davanco, Lei Chen, Robert Newby, Richard Kasica, Kerry Siebein, Liya Yu, Marc Cangemi, Jerry Bowser, and many other people.

I also owe my gratitude to my good friend, Dr. Jason Kestner, who helped me so much in my life. I have also enjoyed many interactions with Dvir Kafri, Vanita Srinivasa, Prabin Adhikari, Xunnong Xu, Xiong-Jun Liu, and many other friends.

I would like to thank the entire dissertation committee for their time and effort to serve on the committee and valuable comments to improve the quality of my dissertation.

This work was supported by the DARPA QuASAR and NSF through the Physics Frontier Center at the Joint Quantum Institute.

Finally, I would like to express my sincere gratitude to my family. Qiuzi Li, my wife, is also a successful physicist. Her love and support are crucial to the completion of my degree. Amelia, my daughter, brings me hope, happiness, and a new motivation for me to work even harder. My parents and parents-in-law are always there for us with deep love and support.

Contents

List of Figures

List of Abbreviations

CMOS	complementary metal-oxide-semiconductor
TQC	topological quantum computation
SPRT	standard platinum resistance thermometer
FBG	fiber Bragg gratings
HCG	high-contrast grating
TE	transverse-electric
SOI	Silicon-On-Insulator
LTO	low temperature oxide
FSR	free spectral range
Q-factor	quality factor
RCWA	rigorous coupled wave analysis
PDH	Pound-Drever-Hall

Chapter 1: Introduction

Photonic sensors are of crucial importance in modern science and technology. They are now fundamental components in various fields including physics, chemistry, engineering, communication, biology, medicine and so on. Photonic sensors can transform optical signals (such as intensity and frequency) into other types of signals (such as electrical voltage), or transform other types of signals into optical signals which can then be processed and analyzed. They can be designed to be ultra-sensitive to certain physical quantities, while robust against other physical parameters. Many photonic sensors are compatible with CMOS technology and can be integrated on chips for use as highly sensitive, small scale and low cost sensors.

Fundamentally, there are 7 physical quantities in nature to be measured, which are length, mass, time, electric current, temperature, amount of substance, luminous intensity. Higher precision and accuracy in the measurement of these fundamental quantities has played crucial roles in the development of physical science. Historically, revolutions in metrology usually come together with revolutions in science.

This thesis focuses on two types of photonic sensors: micro-ring resonator and high-contrast grating membrane based on CMOS technology. I will discuss the fabrication, theoretical basis, experimental characterization of the devices, and their

applications to the measurement of two fundamental physical quantities: temperature and length, as well as some other relevant interesting physical problems.

Chapter 2 presents the study of temperature measurement using ultra-sensitive chip-based micro-ring resonators. Temperature measurements play a central role in modern life ranging from process control in manufacturing [1], physiological monitoring [2, 3], tissue ablation in medicine [4], and environmental control in buildings [5] and automobiles [6]. Despite the ubiquity of thermometers, the underlying technology has been slow to advance over the last century [7]. The standard bearer for accurate temperature measurement, the standard platinum resistance thermometer (SPRT) was initially developed over a century ago [7,8]. Furthermore, many modern temperature sensors still rely on resistance measurements of a thin metal film or wire whose resistance varies with temperature [7]. Though resistance thermometers can routinely measure temperature with uncertainties of 10 mK, they are sensitive to mechanical shock which causes the resistance to drift over time requiring frequent off-line, expensive, and time-consuming calibrations [8].

Recently there has been considerable interest in developing photonic devices as an alternative to resistance thermometers [9–11]. They have the potential to provide greater temperature sensitivity while being robust against mechanical shock and electromagnetic interference. Furthermore, the low weight, small form factor photonic devices might be multiplexed to provide low-cost sensing solutions.

Photonic temperature sensors exploit temperature dependent changes in the properties of a material; typically, a combination of thermo-optic effect and thermal expansion [12–14]. For example, it has demonstrated that the intrinsic temperature

dependence of the refractive index of synthetic sapphire can be exploited for highly sensitive temperature measurement by measuring microwave frequency shifts of the resonant whispering gallery modes of monocrystalline sapphire, with measurement uncertainties of 10 mK from 273.15 K to 373 K [15]. An optical analog of this, using infrared light to probe strain-free fiber Bragg gratings (FBG), exhibits temperature dependent shifts in resonant wavelength of 10 pm/K [9, 10, 12, 13]. This sensitivity has been exploited in commercially available photonic temperature sensors [9,12,13].

However, FBGs are susceptible to strain and are relatively large. Instead, we consider in this thesis the use of ring resonators. In recent years, ring-resonator-based devices [16, 17] have been exploited for bio-chemical sensing applications [18, 19]. In these sensors, temperature-induced shift in the resonance frequency has been a complicating variable or feature that can adversely impact sensor sensitivity and specificity. Indeed, development of an athermal ring resonator is an active area of research [20, 21]. In Chapter 2 we examine their use as thermal sensors, extending the concepts from a recent study by Kim *et al.* [22] that demonstrated that silicon ring resonator devices respond rapidly to small temperature variations (in about 6 μs). Our results indicate that ring resonator based temperature sensors can be used to detect temperature differences as small as 80 μK, a 13-fold improved on previously reported results. This work was done in collaboration with Mohammad Hafezi, Jingyun Fan, Jake M. Taylor, Alan Migdall, Gregory F. Strouse, and Zeeshan Ahmed. We thank Kevin Douglass, Stephen Maxwell, Howard Yoon, Joe Hodges for helpful comments. This work was supported in part by DARPA QuASAR and by the NSF-funded Physics Frontier Center at the JQI, and resulted in a publication [99]

that forms the core of this chapter.

Chapter 3 presents the study of a mirror-in-the-middle system with a high-reflectivity sub-wavelength grating. Dramatic improvements in optical and mechanical design and fabrication enable new regimes of light-matter interactions [27], including observation of long-predicted effects such as cooling to the ground state of a mechanical oscillator [28], ponderomotive squeezing [29–31], and new ultra-sensitive sensors. Of the different approaches, the "membrane in the middle" platform for cavity optomechanics, discussed in Ref. [32] and first demonstrated in Ref. [33] in 2008, is notable for the fact that it decouples the technical demands on the optical and mechanical resonators. It has been used by a number of groups worldwide, for example to observe radiation pressure shot noise [34], demonstrate optomechanically induced transparency [35], generate squeezed light [31], and optically hybridize distinct mechanical modes [36]. In addition, a number of recent theoretical proposals exploit the possibilities inherent in a "membrane in the middle" system with membranes of high reflectivity, including achieving very high optomechanical coupling to the collective modes of an array of such membranes [37, 38], creating interference between adjacent longitudinal cavity modes [39], new approaches to force sensing with sensitivity exceeding the standard quantum limit [40], and studies of quantum nonlinear optics [41]. However, to date, experimental efforts have focused on low-reflectivity membranes, where the perturbations of the cavity modes follow adiabatically with the mechanical motion [33, 42, 43]. In contrast, at high reflectivity, the membrane-mirror effectively divides the cavity into left and right modes [44], leading to the potential for non-adiabatic corrections to the mode

structure with the motion of the membrane and a variety of novel optomechanical phenomena [40, 41, 45–47].

Obtaining high reflectivity with a uniform dielectric membrane is not possible, as one is limited by the Fresnel equations governing reflection at dielectric interfaces as applied to actual materials. High membrane reflectivity can, however, be achieved if the membrane is not uniform but patterned as a photonic crystal structure. It has long been recognized that the reflectivity of such a structure can approach unity at normal incidence [48]. Motivated by these ideas, mechanically compliant photonic crystal structures have been developed in InP [12, 49, 50] and silicon nitride [51]; in the latter case, little or no degradation of the mechanical quality factor was observed. A variant on this approach is provided by a sub-wavelength diffraction grating, in which only zero-order diffraction is allowed and very high reflectivity can be engineered. Such "high-contrast grating" (HCG) structures can be designed with a host of useful properties, including reflectors [52, 53], focusing elements [54, 55], filters, polarizers, and resonators [56].

Here we employ an HCG fabricated in a mechanically compliant silicon nitride membrane to realize a "mirror in the middle" cavity system with a membrane of high reflectivity. We show how the mode structure rapidly changes near the points where the left sub-cavity and right sub-cavity simultaneously come into resonance, and suggest that this is best understood via a perturbation theory starting from unit reflectivity, in contrast to the usual dispersive regime for membrane-in-the-middle work. In addition, the spectral signatures of the system allow more detailed study of the losses than is possible in a simple cavity, and we quantify the reflection,

transmission, absorption and scattering losses in the context of a simple model. This work was done in collaboration with Utku Kemiktarak, Corey Stambaugh, Jacob Taylor, and John Lawall. Research performed in part at the NIST Center for Nanoscale Science and Technology, resulting in the publications [98, 100] that form the core of this chapter.

We use the mirror-in-the-middle cavity for highly sensitive and accurate displacement sensing in Chapter 4. The modern definition of the fundamental unit meter is the length of the path traveled by light in vacuum during a time interval of 1/299792458 of a sencond [70]. By definition, the accuracy of distance measurement is limited fundamentally by the accuracy of time measurement, which currently has an accuracy of the order of 10^{-18} using an atomic clock [71, 72]. Given the ability to accurately measure the time, it is natural to use light as a ruler, which has a universal constant velocity in vacuum [73]. A direct application is the measurement of the distance between the moon and the earth [74–77].

One widely used methodology for measuring small differential distance is two-beam amplitude splitting interferometer [78]. The resolution of an interferometer is the minimum detectable displacement. For a two-beam amplitude splitting interferometer, the laser is split into two beams, one to a reference mirror, and the other to the target, and the reflected beams are then combined to interfere with each other, giving a sinusoidal optical signal as a function of the displacement. Commercial interferometers can give sub-nanometer resolution.

Generally, the two-beam amplitude splitting interferometric displacement measurements require calibration in order to determine the displacement from the elec-

tric output signal, and is susceptible to noise in the reference arm. Another type of high resolution interferometer is the Fabry-Perot interferometer which is independent of an external reference arm. Fabry-Perot interferometers are used to measure, e.g., small displacement inside tunneling microscope [80] and gravitational constant [81, 82]. An absolute uncertainty below 10 pm has been achieved by John Lawall [83].

Here we use the mirror-in-the-middle system as a platform for high resolution absolute displacement measurement, based on radio frequency measurement without an optical reference. We have achieved a resolution of 4×10^{-14} m at a sampling rate of 10 Hz. This displacement sensing is used to analyze the stability and slow movement of the grating membrane in the mirror-in-the-middle cavity system. This work was done in collaboration with Utku Kemiktarak, Jacob Taylor, and John Lawall.

We propose buckling transition experiments for future study of optomechanics using the grating membrane in Chapter 5. The radiation pressure force induces a change in the dynamics of optomechanical systems, which has applications such as cooling to the ground state of a mechanical oscillator [28], ponderomotive squeezing [29–31], and enhancing the sensitivity of gravitational wave detectors [84, 85]. A stable optical trap for a gram-scale mirror has been reported, where the effective optical spring constant is orders of magnitude larger than the low frequency mechanical mode [86]. At larger light intensities when red detuned, the original equilibrium position becomes unstable and the effective optical spring potential may transit into a double well potential, which leads to optical bistability [87]. Here we study

theoretically two types of buckling transitions due to the optomechanical interaction between light and a grating membrane. The buckling transition can be observed using our displacement sensing technique. This work was done in collaboration with Jacob Taylor and John Lawall.

The appendices A and B are about fabrication of the micro-ring resonator and grating membrane. It has been reported in [88–90] that micro-ring resonator lattice can support topological states. Ref. [91, 92] are the theoretical works performed during my graduate study on topological physics and topological quantum computation.

Chapter 2: Ultra-sensitive chip-based photonic temperature sensor using ring resonator structures

2.1 Overview

Resistance thermometry provides a time-tested method for taking temperature measurements. However, fundamental limits to resistance-based approaches have produced considerable interest in developing photonic temperature sensors to leverage advances in frequency metrology and to achieve greater mechanical and environmental stability. Here we show that silicon-based optical ring resonator devices can resolve temperature differences of 1 mK using the traditional wavelength scanning methodology. An even lower noise floor of 80 μK at 1 Hz for measuring temperature difference is achieved in the side-of-fringe, constant power mode measurement.

2.2 Ring Resonator based Thermometer

The temperature dependence of the ring resonator arises from temperature-induced changes in the refractive index and in the physical dimensions of the ring. Fig. 2.1 shows a typical ring resonator. Let us assume the coupling between the waveguide and the ring to be lossless without back scattering. The coupling is

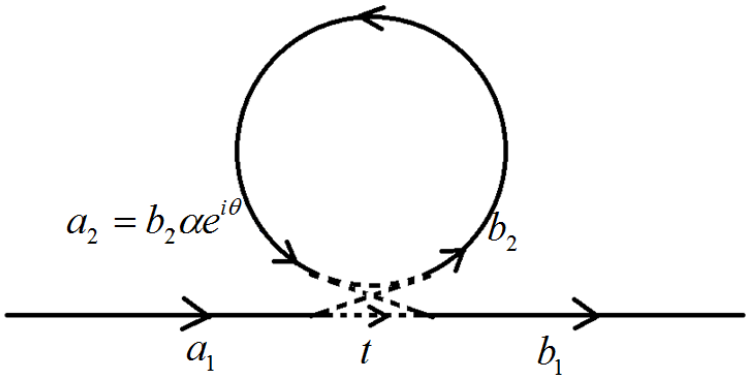

Fig. 2.1: Geometry of a ring resonator. t is a coupling parameter describing the coupling between the ring and the straight waveguide, α describes the loss of laser per round-trip in the ring, and θ is the phase gained per round-trip.

described by the following equation,

$$\begin{pmatrix} b_1 \\ b_2 \end{pmatrix} = \begin{pmatrix} t & \kappa \\ -\kappa^* & t^* \end{pmatrix} \begin{pmatrix} a_1 \\ a_2 \end{pmatrix}, \tag{2.1}$$

where t and κ are coupling constants satisfying $|t|^2 + |\kappa|^2 = 1$. Without loss of generality, we assume t to be a real number. a_2 and b_2 are related by

$$a_2 = b_2 \alpha e^{i\theta}, \tag{2.2}$$

where α describes the loss of light per round-trip in the ring, and θ is the phase gained per round-trip. Solving Eq. (2.1) and Eq. (2.2), we obtain the transmission factor,

$$\frac{|b_1|^2}{|a_1|^2} = \frac{\alpha^2 + t^2 - 2\alpha t \cos\theta}{1 + \alpha^2 t^2 - 2\alpha t \cos\theta}, \tag{2.3}$$

which is the ratio of output power to input power.

$$\theta(\lambda, T) = \frac{n(\lambda, T) L(T) 2\pi}{\lambda} = \frac{n(\lambda, T) L(T) 2\pi f}{c}, \tag{2.4}$$

where f is frequency of the laser, λ is the vacuum wavelength, n is the effective refractive index, L is the perimeter of the ring, and T is the temperature. Resonance occurs at $\theta_m = 2m\pi$, when the output is at its minimum. The resonance wavelength is

$$\lambda_m = \frac{n(\lambda_m, T)L(T)}{m}, \tag{2.5}$$

where m is the mode number. The free spectral range is

$$\Delta f_{FSR} = \frac{c}{n(\lambda_m, T)L(T)}. \tag{2.6}$$

When $\alpha = t \approx 1$, the minimum output goes to 0, and the full frequency width at half maximum is

$$\Delta f_{FWHM} = \frac{(1-t^2)c}{\pi n(\lambda_m, T)L(T)}. \tag{2.7}$$

The quality factor is

$$Q = \frac{f}{\Delta f_{FWHM}} = \frac{\pi n(\lambda_m, T)L(T)}{(1-t^2)\lambda_m} \tag{2.8}$$

When the temperature changes, the resonance wavelength also varies. The temperature-induced shift in wavelength is given by

$$\Delta\lambda_m = \frac{\partial_T n + n\partial_T L/L}{n - \lambda_m \partial_{\lambda_m} n}\lambda_m \Delta T, \tag{2.9}$$

where $n - \lambda_m \partial_{\lambda_m} n$ is the group index.

By measuring the resonance wavelength, we can detect the variation in temperature. Note that the variation in the refractive index due to the thermal expansion coefficient for silicon (3.57×10^{-6}/K) is a factor of 100 smaller than that of the estimated thermo-optic effect (2×10^{-4}/K) of the silicon waveguide and not included

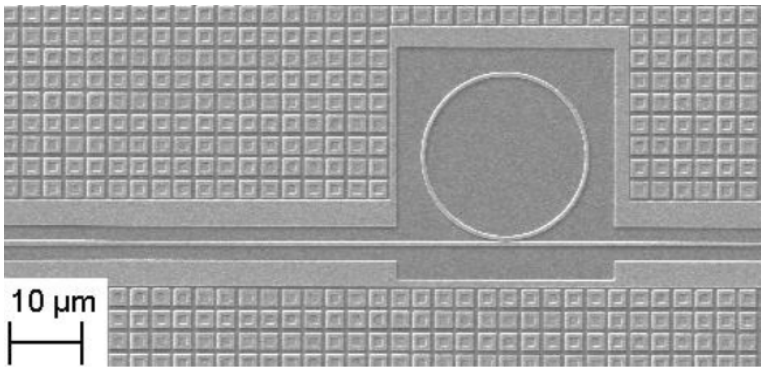

Fig. 2.2: SEM image of a ring resonator device (11 μm radius, 130 nm gap).

in our analysis of the performance of ring resonator devices. Fig. 2.2 depicts a schematic of the photonic device (fabricated by ePIXfab) consisting of a ring resonator coupled to a straight-probe waveguide, with cross-section designed to be 610 nm×220 nm to assure single-mode propagation of the transverse-electric (TE) light (the electric field in the slab plane) at the telecom wavelengths (1550 nm) and air gap of 130 nm for evanescent coupling between the resonators and the probing waveguide.

2.3 Measurement

Fig. 2.3 shows the setup of our experiment. A tunable Santec laser (TSL-210) was used to probe the ring resonator. A small amount of laser power was immediately picked up from the laser output for wavelength monitoring (HighFinesse WS/7) while the rest, after passing through the photonic device, was detected by a large sensing-area power meter (Newport, model 1936-R). The photonic chip itself is mounted on a 2-axis stage (Newport) in a two-stage temperature controlled

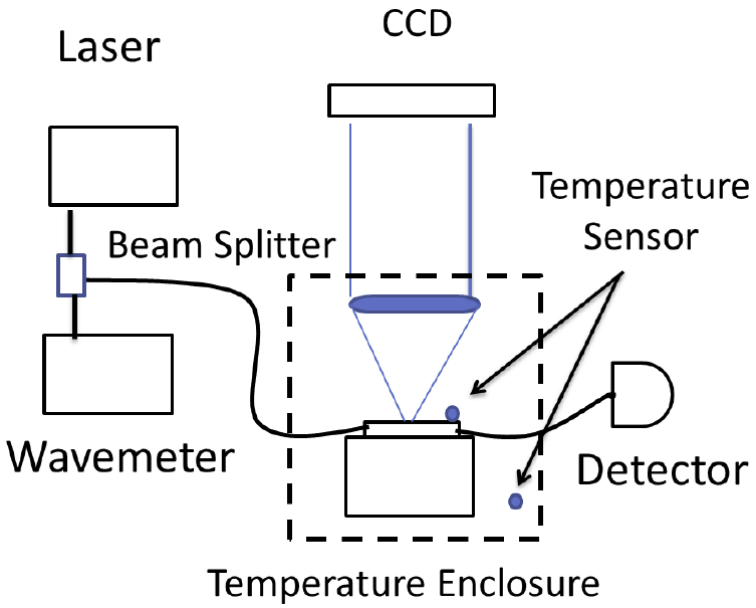

Fig. 2.3: Block diagram of the two microscopy-based interrogation setup used to study the photonic devices.

enclosure. Input from a platinum resistance thermometer from each stage is fed to its respective proportional-integral-derivative controller that drives a thermoelectric cooler (Laird Technologies). The first stage minimizes global temperature fluctuations inside the enclosure to better than ± 1 K, while the second stage minimizes temperature variations at the chip to ≤ 17 mK over 24 hours. The relative humidity (%RH) levels inside the temperature enclosure were monitored using a portable humidity meter (Vaisala). Relative humidity levels were varied inside the enclosure by varying the flow rate of water saturated air.

Traditionally, photonic thermometers such as those based on Fiber Bragg gratings (FBG) employ continuous wavelength scanning techniques to measure temperature changes [13]. In this scheme - Wavelength Scanning mode - the probe laser is continuously scanned across the frequency region of interest and the trans-

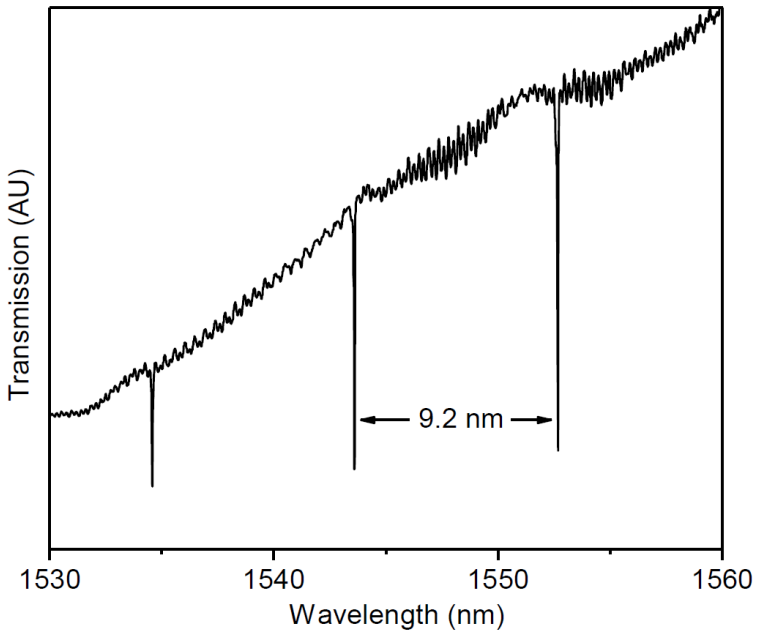

Fig. 2.4: The 11 μm radius ring resonator used here shows an FSR of $\approx$ 9.2 nm near 1550 nm.

mission/reflection spectrum is recorded and its center frequency computed. With the help of a previously determined calibration curve, the center frequency is then converted to temperature. Using this approach we evaluated our ring resonator based temperature sensor by systematically varying the temperature between 288 K and 306 K. Our measurements of a resonator with ring radius of 11 μm and a gap of 130 nm, show a free spectral range (FSR) of ca. 9.2 nm and bandwidth of 0.03 nm corresponding to a quality factor (Q-factor) of 52000 (see Fig. 2.4). As shown in Fig. 2.5, we observed that this device shows a temperature dependent shift in resonance wavelength of 77 pm/K, which is an eight-times improvement over FBG temperature sensor. Given the wavelength resolution of 0.1 pm for the wavemeter used in the current setup, we estimate that this temperature sensor can

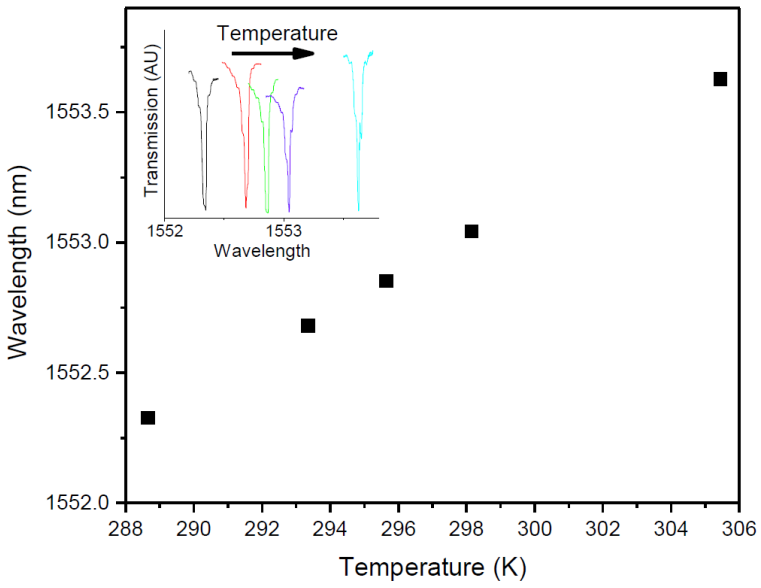

Fig. 2.5: The ring resonator acts as a notch filter whose resonance window is sensitive to temperature changes. The resonance wavelength systematically increases as the temperature increases; resonances at various temperatures are shown in the insert.

resolve temperature differences of ≈1 mK.

Humidity and intrinsic heating are known to often affect the optical response of photonic sensors [23, 24]. We systematically examined the impact of relative humidity (%RH) changes on resonance frequency by varying humidity levels from 17%RH to 26%RH at 294.15 K. These measurements do not show any significant changes in resonance frequency as %RH is varied. We note that at 294.15 K, an increase of Δ(%RH)= 9 would require a temperature increase of ≈9 K. Our measurements indicate the change in resonance frequency observed in Fig. 2.5 derives from temperature changes and is not correlated to changes in humidity. The insensitivity of our device to changes in humidity likely derives from the passivating

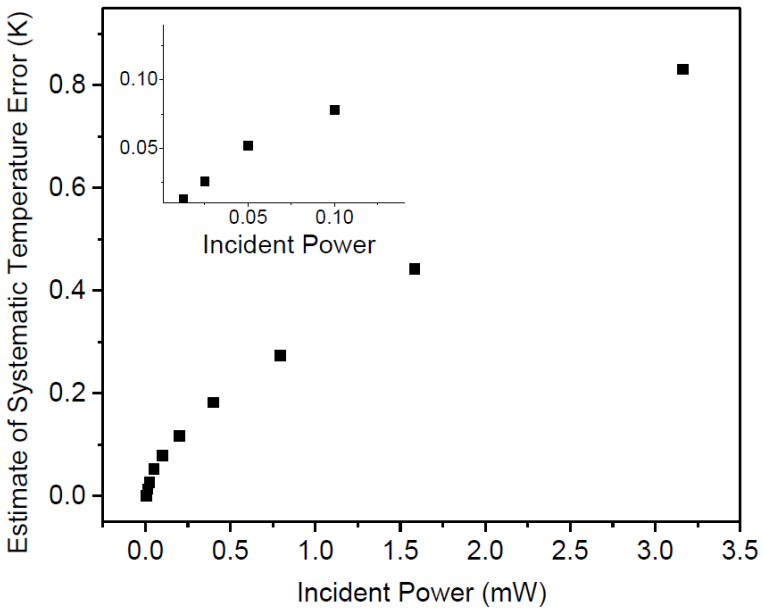

Fig. 2.6: Increasing incident laser power causes self-heating in ring resonator based devices resulting in an increase of the device resonance wavelength. Consequently, ring resonator increasingly over-estimates the ambient temperature compared to a platinum resistance thermometer. Over the incident power range of 0.0063 mW to 0.1 mW the estimated systematic temperature error is below 0.1 K.

SiO2 layer deposited on-top of the ring resonator. In contrast to the observed insensitivity to humidity changes, we find that varying the input laser power from 0.0063 mW to 3.16 mW results in a systematic upshift in the resonance frequency and a corresponding systematic error in temperature determination (see Fig. 2.6). As shown in Fig. 2.6, as the incident laser power is increased, the ring resonator increasingly over-estimates the ambient temperature as compared to the platinum resistance thermometer located on the chip stage. Our results suggest that incident laser power fluctuations, if left unaccounted for, may be a significant source of

measurement uncertainty. The impact of laser induced self-heating, however, might be mitigated by operating at low laser powers ($\leq$ 12 μW) or by ensuring the operating laser power matches the laser power used during device calibration of the sensor.

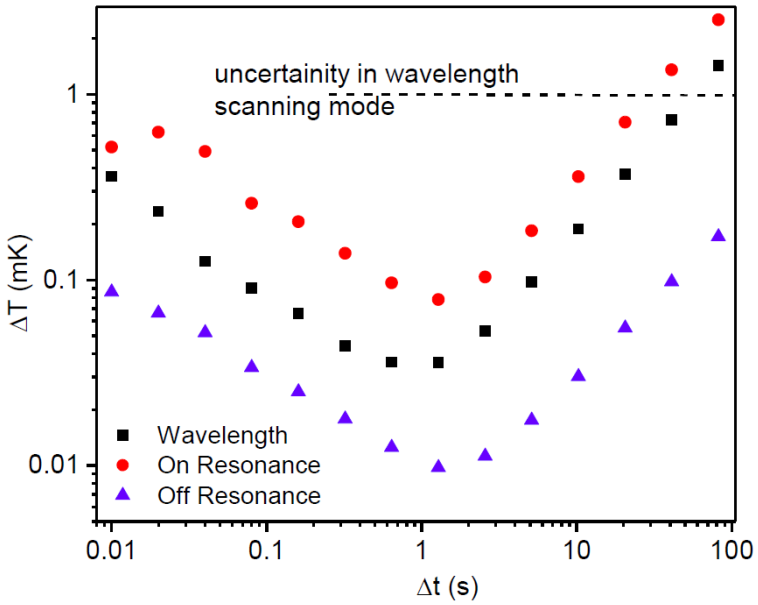

Fig. 2.7: Allan Variance measurements indicate the instrument noise bottoms out at a 1 Hz measurement rate, creating a noise floor of ≈80 μK.

Noise Source	Noise Level (μK)
Laser Power	10
Laser Frequency	40
Background thermal fluctuations	69

Tab. 2.1: Noise sources contributing to photonic temperature measurement

Here we demonstrate an alternative approach to Wavelength Scanning mode

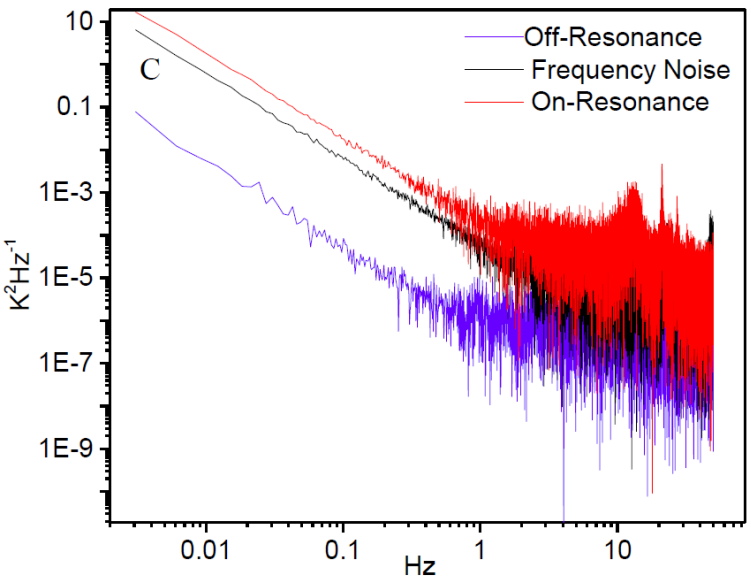

Fig. 2.8: Power spectral density plot shows $1/f$ noise dependence.

for measuring temperature changes smaller than 1 mK. In this measurement scheme – side of fringe, constant power mode – the laser power is maintained at a constant power level and its frequency centered on the side of resonance at the point of steepest descent (point of half contrast). A small, temperature-dependent shift in resonance frequency results in a large change in transmitted laser intensity. Since the resonance lineshape is known, intensity fluctuations can be converted to an estimate of center frequency change without measuring the peak shape. This measurement scheme is limited by the system noise including both laser frequency and intensity noise, as shown in Fig. 2.7. We have quantified the system noise at 296.15 K by systematically measuring the output power of the ring resonator as a function of time with laser wavelength set on- and off-resonance (Tab. 2.1). The laser frequency was simultaneously monitored during these measurements to quantify laser frequency noise which primarily derives from long term drift in laser frequency. To

quantify this, we performed a control, off-resonance measurement in which the laser is tuned in between two resonance peaks; transmitted intensity corresponds to light traveling through the entire optical train except the on-chip resonator. This control measurement allows us to estimate noise sources deriving from fluctuations in laser power and light coupling. The side-of-fringe approach is estimating the resonance frequency by local inversion of the expected lineshape, and thus contains additional contributions from background thermal fluctuations and laser frequency noise. With the data sampling rate set at 100 Hz, a total of 32,768 data points were collected for each measurement. This data set was used to generate the noise power spectral density spectrum [25] and the corresponding Allan variance plot [14] (Fig. 2.7 and Fig. 2.8). Our results indicate that Allan variance reaches a minimum at sampling rate of ≈1 Hz. At 296.15 K, the noise floor on the temperature measurement of ≈80 μK at 1 Hz is set by on-resonance measurement, which represents a 13-fold improvement over the traditional wavelength scanning mode. The on-peak measurement contains contributions from laser power noise (≈10 μK), laser frequency noise (≈40 μK) and additional technical noise which we attribute to background thermal fluctuations (≈69 μK). The background thermal fluctuations contain contributions from thermorefractive noise arising due to intrinsic temperature fluctuations in the active device region due to its small size. Using the thermodynamic equation [26] ($< \mu^2 >= k_b T^2/CV\rho$), where T is the temperature of the environment, k_b is the Boltzmann constant, ρ is the density and C is the specific heat capacity at constant volume of the material (≈700 J·Kg/K for Silicon), for this finite size device (0.22μm×1.2μm×66μm circumference) the expected intrinsic temperature

fluctuation is ≈100 μK. However, over the millisecond-to-second averaging times used in the measurement, the effective volume of the device is substantially larger due to heat exchange with the insulating substrate. We expect our measured value to be due to other sources of fluctuations. At time scales of 1 min or longer (time required for scanning the resonance peak), the noise floor for side-of-fringe mode rises above the uncertainty level in wavelength scanning mode. Our results suggest that for measurement applications requiring long observation times (e.g. process control), in the absence of frequency stabilization, the classic wavelength scanning mode provides lower measurement uncertainty. The side of fringe constant power mode is best suited for dynamic temperature measurements.

2.4 Conclusions

We have demonstrated in this chapeter that ring resonators can be used for temperature sensing with sub-mK resolution. Using the traditional wavelength scanning methodology, we demonstrate the temperature sensitivity of ring resonator based devices is a factor of eight greater than FBG based devices. We have demonstrated that the novel use of "side of fringe, constant power mode" allows us to detect temperature differences of 80 μK. This represents a 13-fold improvement in temperature sensing as compared to wavelength scanning methodology. The noise level of these devices can be further reduced by laser frequency and power stabilization techniques. The low noise levels of these photonic sensors along with their low thermal mass and immunity to electromagnetic interference make them

attractive choice for applications in aerospace and microfluidics. However, key systematic errors induced by laser power and laser frequency noise remain to be addressed over a wider range of temperature and operating environments.

Chapter 3: From membrane-in-the-middle to mirror-in-the-middle with a high-reflectivity sub-wavelength grating

3.1 Overview

We demonstrate a "membrane in the middle" optomechanical system using a silicon nitride membrane patterned as a subwavelength grating. The grating has a reflectivity of 0.9981 ± 0.0001, effectively creating two sub-cavities, with free spectral ranges of 6 GHz, optically coupled via photon tunneling. Measurements of the transmission and reflection spectra show an avoided crossing where the two sub-cavities simultaneously come into resonance, with a frequency splitting of 54 MHz. We derive expressions for the lineshapes of the symmetric and antisymmetric modes at the avoided crossing, and infer the grating reflection, transmission, absorption, and scattering through comparison with the experimental data.

3.2 High-Contrast-Grating (HCG) Design

The HCG design was driven by the desire for a structure that would be relatively insensitive to fabrication parameters while offering high reflectivity. Although analytic formulations for HCG properties are available for idealized geometries [58],

we have relied on rigorous coupled wave analysis [59] (RCWA), which allows more general structures to be treated [57]. Low-stress silicon nitride, with an index of refraction of $n \approx 2.2$, and a thickness of $t = 470$ nm, is found to allow high reflectivity at our target wavelength of 1560 nm with grating periods in the range of $1.44\,\mu$m to $1.54\,\mu$m and finger widths in the range of $0.52\,\mu$m to $0.62\,\mu$m. In earlier work [60], the imaginary part of the index of refraction of the silicon nitride membranes was found to be in the range $1.66\times10^{-5} < n_I < 1.92\times10^{-5}$. Taking $n_I = 1.8\times10^{-5}$, the calculation shows the absorption of the HCG structure to be in the range of 1.3×10^{-4} to 1.5×10^{-4} when it is illuminated from one side, depending on the exact geometry. The unpatterned membrane, on the other hand, is found to have an absorption of 6.3×10^{-5}; the difference is the consequence of electric field enhancement inside the HCG structure. Fig. 3.1 shows an example of the grating membranes we have fabricated in the clean room at NIST (see Appendix B for details of the fabrication process).

3.3 Model for "HCG in the middle" system

We model the "HCG in the middle" system (as shown in Fig. 3.2) by means of the transfer matrix formalism, which yields the steady-state solution for the fields within and outside the cavity [62]. Each element in the cavity is represented as a two-port device, in which the complex amplitudes of the outgoing and ingoing electric fields on the right are related to the ingoing and outgoing fields on the left

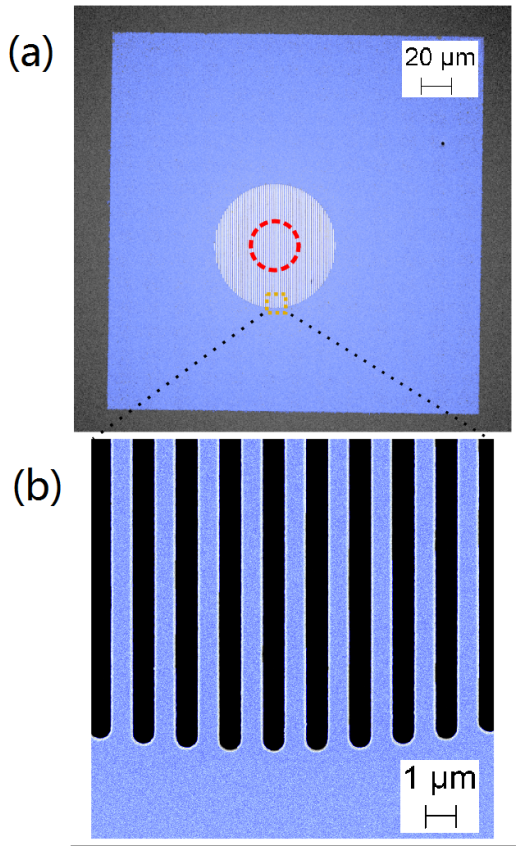

Fig. 3.1: SEM images of a silicon nitride membrane (250 μm×250 μm) with pattered HCG. The HCG has a diameter of 80 μm, and the small red circle represents the size (waist $\omega_0 = 17\,\mu$m) of the confined cavity mode.

by means of a matrix M, as follows:

$$\begin{pmatrix} E_{out} \\ E_{in} \end{pmatrix}_R = M \begin{pmatrix} E_{in} \\ E_{out} \end{pmatrix}_L .$$

The cavity length is denoted $2d$, and the membrane is positioned a distance $d + x$ from the input coupler (left mirror) of the cavity, as shown in Fig. 3.2. The transfer matrix M^{cav} for the entire cavity can be found by simple matrix multiplication of the transfer matrices of the individual elements, and the cavity transmission and reflection coefficients are given by $t_{cav} = 1/M_{22}^{cav}$ and $r_{cav} = M_{21}^{cav}/M_{22}^{cav}$.

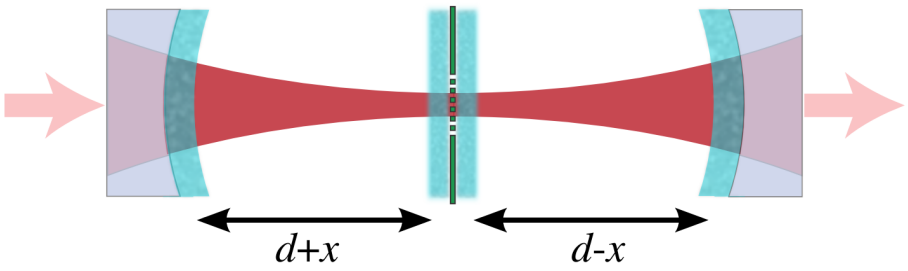

Fig. 3.2: The highly-reflective membrane is located near the center of an optical cavity. It is represented as a zero-thickness slab of polarizable material sandwiched between two "scattering" elements (light blue rectangles), each of which attenuates the field in an optical traveling wave by $e^{-S_m/4}$. The dielectric cavity mirrors are modeled as lossless ($R + T = 1$) reflecting elements, next to which similar "scattering" elements, characterized by S_{diel}, are placed. The cavity is nearly concentric, resulting in a small beam waist.

The starting point for our description of the optical properties of the membrane is that taken by Spencer and Lamb [63] and others [64, 65] in early studies of two coupled lasers, as well as more recent theoretical studies and proposals in optomechanics [32, 37, 38]. The membrane is taken to be a zero-thickness slab of dielectric material with complex polarizability $\zeta = \zeta_R + i\zeta_I$, such that the reflection and transmission coefficients are $r'_m = i\zeta/(1 - i\zeta)$ and $t'_m = 1/(1 - i\zeta)$, respectively. The corresponding transfer matrix is [37]

$$M_{mem} = \begin{pmatrix} 1 + i\zeta & i\zeta \\ -i\zeta & 1 - i\zeta \end{pmatrix}. \tag{3.1}$$

Material absorption is described by $\zeta_I > 0$; it is readily shown that $|r'_m|^2 + |t'_m|^2 = 1$ if and only if $\zeta_I = 0$. While this model is clearly an idealization of the HCG,

neglecting its thickness and resonant properties, it does capture the essence of the device for these purposes.

Nevertheless, a somewhat more general model is required to account for loss mechanisms other than absorption, such as scattering from surface roughness. Indeed, if we consider light incident from only one side of the membrane described by (3.1), the fraction of the incident power lost to absorption is simply $A_m = 1-|r'_m|^2-|t'_m|^2$. If, however, light is incident from both sides, of the same amplitude but differing in phase by θ, the fraction of the incident power lost to absorption is found to be

$$\frac{P_{in}-P_{out}}{P_{in}} = \frac{2\zeta_I(1+\cos\theta)}{\zeta_R^2+(1+\zeta_I)^2}\,.$$

The power absorbed vanishes even if $\zeta_I \neq 0$ for $\theta = \pi$, meaning that the membrane is located at a node of the electromagnetic field. In order to model losses from other mechanisms, we sandwich the membrane between two "scattering" elements (Fig. 3.2), each of whose transfer matrix is taken to be

$$M_{scat} = \begin{pmatrix} e^{-S_m/4} & 0 \\ 0 & e^{S_m/4} \end{pmatrix}, \tag{3.2}$$

where $S_m << 1$. The effect of this matrix is to attenuate the transmitted field by a factor $e^{-S_m/4}$ in a single pass, and thus the power by a factor $e^{-S_m/2}$. For single-sided illumination, then, the fractions of the incident power reflected and transmitted are $R_m = |r'_m|^2 e^{-S_m}$ and $T_m = |t'_m|^2 e^{-S_m}$, respectively, and one finds $R_m + T_m + A_m + S_m = 1$.

For simplicity, we use the latter formalism to describe losses in the cavity mirrors as well. We model each dielectric cavity mirror as a lossless reflector, with

real reflection and transmission coefficients r and t satisfying $r^2 + t^2 = 1$, next to which a similar scattering element parametrized by S_{diel} is located (Fig. 3.2). The assumption that the mirrors have equal reflection and transmission is reasonable, given that they were produced in the same coating run. The assumption of equal scattering losses will be discussed subsequently.

3.4 Experiment Setup

The optical cavity used in our experiment is comprised of two high-reflectivity dielectric mirrors with nominal radii of curvature $\mathcal{R}_{diel} = 25$ mm. The cavity length is set such that the optical cavity is nearly concentric, with a cavity length approximately 28 ± 6 μm below the stability boundary of $2\mathcal{R}_{diel}$ [66]. The geometry of the confined mode has a spot size (radius) on the mirrors of $\omega_1 = 730 \pm 40$ μm and a waist (radius) of $\omega_0 = 17 \pm 1$ μm; the numeric value following the $\pm$ sign is the combined standard uncertainty given with a confidence level of approximately 68%. This choice of waist is motivated by a compromise between minimizing beam spillage off of the patterned grating, and having a waist whose wavevectors have a narrow distribution of transverse momenta, as noted previously [61].

The membrane is placed on a X-Y-Z stage with tip/tilt control so that it can be positioned at the center of the optical cavity. It is adjusted to be normal to the cavity mode and located at the mode waist by monitoring the transmission, and minimizing signatures of coupling from the TEM_{00} mode to higher-order transverse modes. The mode-matching optics are not readjusted after the membrane is inserted into the

optical cavity. The longitudinal location is confirmed by blocking the portion of the cavity following the membrane so as to establish a simple Fabry-Perot cavity with the input coupler and the HCG, and measuring its free spectral range (FSR). The FSR of this sub-cavity is a factor of two larger than that of the empty cavity (membrane removed); accounting for measurement uncertainty, we infer that the membrane is within 2.3 μm of the center of the cavity.

3.5 Empty Cavity

We begin by studying the cavity in the absence of an HCG in order to establish the characteristics of the cavity mirrors. In Fig. 3.3 the measured transmission of the empty cavity is plotted on a logarithmic scale. The large peak is the transmission of a fundamental TEM_{00} mode, and sets the origin of the detuning. The small peaks, with amplitudes two orders of magnitude below that of the TEM_{00} mode, are due to coupling to higher-order transverse cavity modes. Their small size indicates that the injected beam is well, but not perfectly, mode-matched to the cavity. Moreover, the frequencies of the higher-order modes are related to the overall cavity length and geometry of the confined modes [66]; in particular, one infers that the waist size of the fundamental mode is $\omega_0 = 17\,\mu$m, as noted previously.

In Fig. 3.4, the calibrated cavity transmission and reflection of a TEM_{00} resonance are plotted on a linear scale. The frequency scale was established by means of an auxiliary experiment using sidebands on the laser provided by an electro-optic modulator. The predicted transmission and reflection spectra,taking $\zeta \to 0$ in our

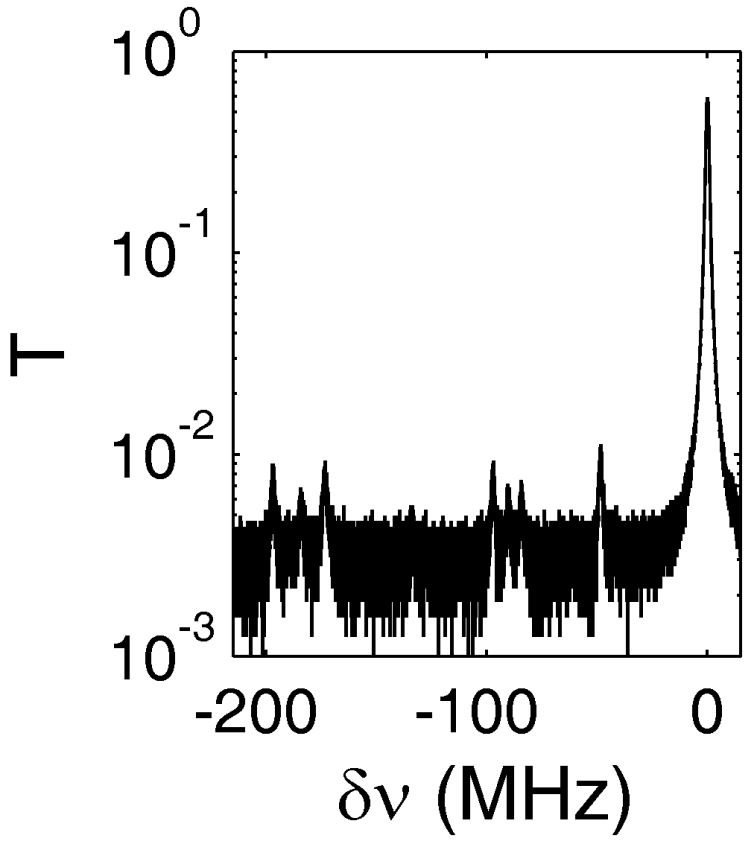

Fig. 3.3: Transmission spectrum of the empty cavity, logarithmic scale. The large peak corresponds to a TEM_{00} mode, and the small peaks are higher-order transverse modes. Their small size relative to the main peak is indicative of good mode matching.

model, are

$$T_{cav}^{00} = \frac{P_t}{\epsilon P_{in}} = \frac{T^2}{(S_{diel}+T)^2 + \left(\frac{2\pi\delta\nu}{\Delta\nu}\right)^2} \tag{3.3}$$

$$R_{cav}^{00} = \frac{P_r - (1-\epsilon)P_{in}}{\epsilon P_{in}} = 1 - \frac{T^2 + 2TS_{diel}}{(S_{diel}+T)^2 + \left(\frac{2\pi\delta\nu}{\Delta\nu}\right)^2}. \tag{3.4}$$

Here $T = t^2$ is the (power) transmission of the input and output couplers, $\Delta\nu \equiv c/(4d)$ is the free spectral range of the cavity (length $2d$), and $\delta\nu = \nu - \nu_0$ is the detuning of the incident light with frequency ν from the cavity resonance frequency

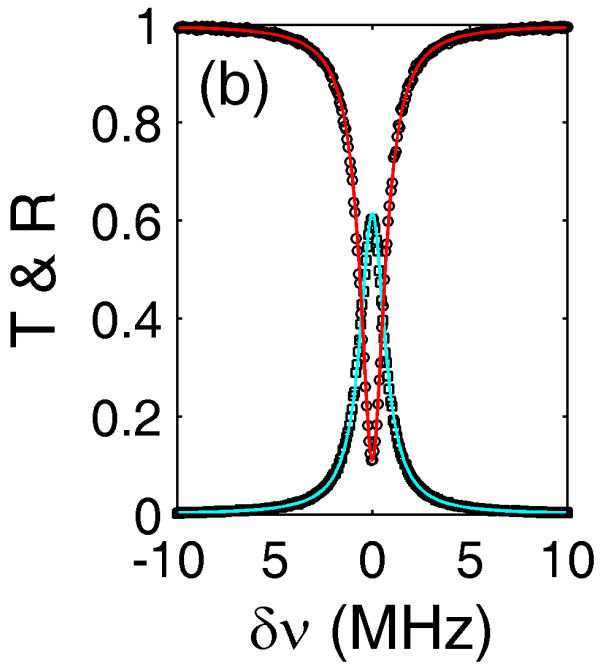

Fig. 3.4: Transmission (cyan) and reflection (red) for the empty cavity, with Lorentzian fits. From these data the characteristics of the cavity mirrors can be determined.

ν_0. As discussed by Hood et al [67], the spectra of the TEM_{00} mode are related to the experimentally determined transmitted power P_t and reflected power P_r by means of a factor ϵ which is equal to the fraction of the input power coupled into the TEM_{00} mode. The FWHM of the transmission peak is

$$\frac{\kappa}{2\pi} = \frac{S_{diel} + T_{avg}}{\pi}\Delta\nu. \tag{3.5}$$

By fitting the data in Fig. 3.4 to (3.3) and (3.4), we determine $S_{diel} = (3.0 \pm 0.1) \times 10^{-4}$, $T = (1.30 \pm 0.04) \times 10^{-3}$ and $\epsilon = 0.92 \pm 0.005$. In the foregoing analysis, it was not actually necessary to assume equal scattering losses for the input and output couplers; the quantity S_{diel} in fact yields the average of the two. Alternatively put,

it is not possible to separately infer the scattering losses of the two mirrors of the empty cavity in our model. It is thus natural at this point to make the assumption that they are equal. Having established the characteristics of the empty cavity, we are now in a position to study the cavity with an HCG in the middle.

3.6 HCG In Cavity

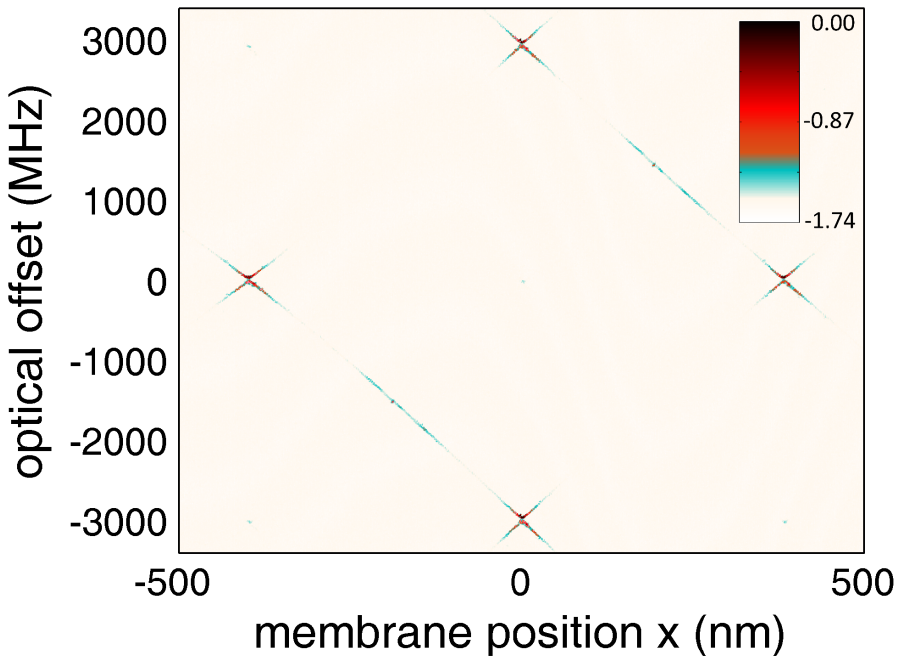

Fig. 3.5: The transmission is large only at points x where both left and right sub-cavities can be simultaneously resonant. The color scheme is logarithmic, with the colorbar representing $\log_{10}(T)$.

When a highly reflective HCG membrane is placed in the center of the cavity, the system behaves as two sub-cavities that are optically coupled through the membrane transmission and mechanically coupled through the position of the membrane. The transmission and reflection spectra are then functions of the axial membrane

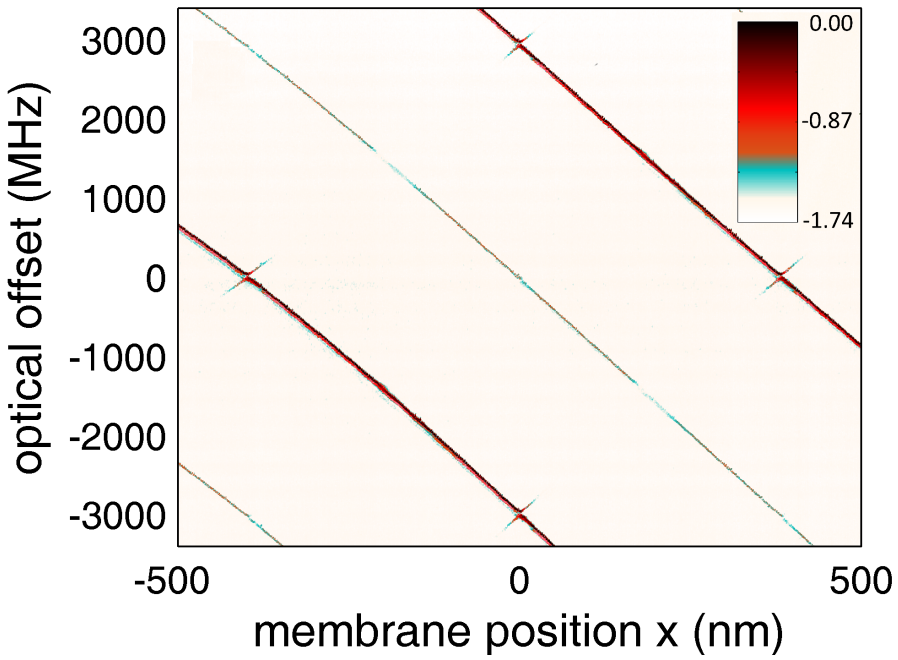

Fig. 3.6: The reflection exhibits a pronounced dip for all frequencies such that the left (input) sub-cavity is resonant. The weaker reflection dip arises from TEM_{10} modes that have not been suppressed. Here the color scheme represents $\log_{10}(1-R)$. The anti-crossings result from the coupling between the left and right cavity modes.

position. The transmission, Fig. 3.5, is largely maximized when each sub-cavity is simultaneously resonant, which is possible when $x \approx N\lambda/4$. The reflection, on the other hand, exhibits a deep dip whenever the left-hand sub-cavity is resonant, as shown in Fig. 3.6. Qualitatively, this can be understood as the left-hand sub-cavity being approximately impedance matched [68]. At the points where the transmission is maximal, there are in fact pronounced avoided crossings in the spectra, as shown in Figures 3.7. (The distortion of the lower branch of the resonance curves at $x \approx 4$ nm is due to the presence of higher-order transverse modes). At the avoided crossing at

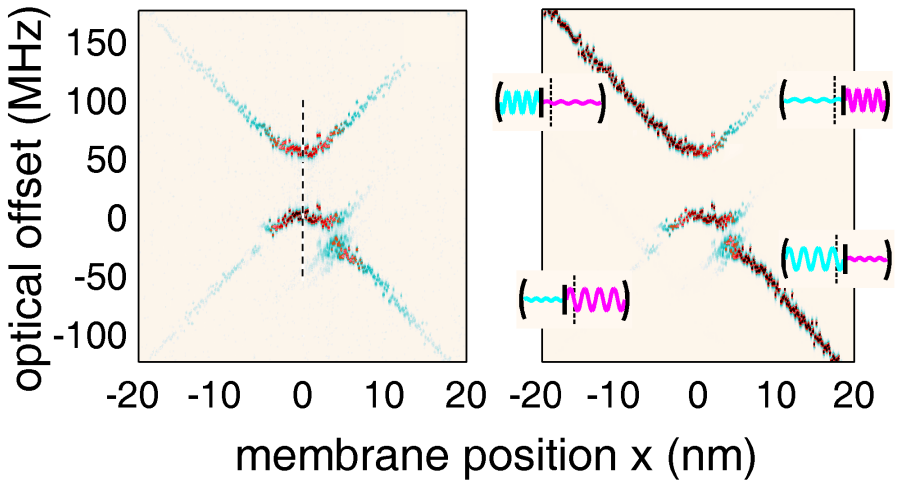

Fig. 3.7: Left: Fine scan of transmission near the normal mode splitting. The crossing seen at $x \approx 4$ nm results from the TEM_{02} symmetric mode coupling to the antisymmetric TEM_{00} mode. The dashed line at $x = 0$ indicates the data slice plotted in Fig. 3.9(a). Right: Zoom in on the reflection data; the insets represent the field distribution. The illustrations near the upper (lower) branch are associated with the symmetric (antisymmetric) modes.

$x = 0$, the lower resonance corresponds to an optical cavity mode with odd parity, and the upper resonance corresponds to an optical mode with even parity (Fig. 3.8). For $x \neq 0$, the mode amplitudes in the two sub-cavities are different, and the modes are no longer purely symmetric or antisymmetric. For $-\lambda/8 < x < 0$, the higher-frequency mode is localized primarily in the left sub-cavity, while for $0 < x < \lambda/8$, it is the lower-frequency mode that is localized to the left. This is illustrated in the close-up of the reflection spectrum shown in Fig. 3.7. Analytic expressions for the modes of a lossless cavity, with perfectly reflecting cavity mirrors and $\zeta_I \to 0$, have been given previously [64, 65].

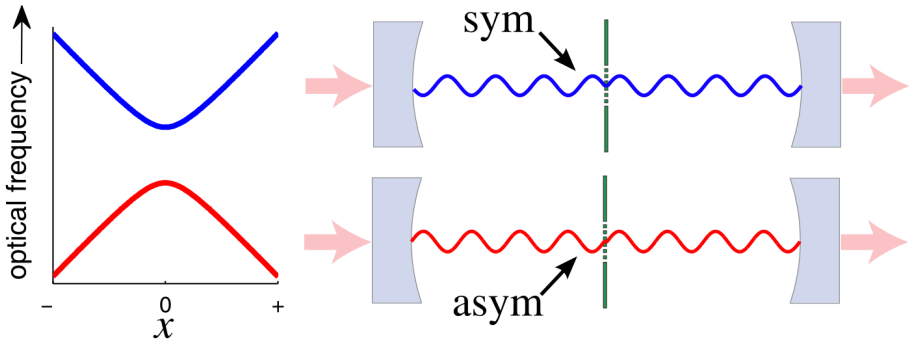

Fig. 3.8: Normal mode splitting. In the vicinity of membrane positions x such that left and right sub-cavities are simultaneously resonant, the cavity modes split into a doublet whose elements have opposite parity about the membrane.

In our model of a zero-thickness membrane, the field amplitude of the antisymmetric mode vanishes at the membrane location, and the wavelength of the mode is the same as that of the empty cavity at the same frequency. The symmetric mode, however, is nonvanishing, with a discontinuous spatial derivative at the membrane position [64]. As $R_m \equiv |r_m|^2 \to 1$, the field amplitude at the membrane diminishes and approaches a node, but as long as $R_m < 1$ the amplitude will be nonzero and result in absorption. Similarly, the phase accumulation from $-d$ to d remains larger than that for the antisymmetric mode, with the consequence that the frequency is higher. We denote the frequency difference between the symmetric and antisymmetric modes at $x = 0$ as $\delta\nu_{SA}$.

The transmission and reflection spectra, accounting for cavity and membrane losses, are given by our transfer matrix treatment. Here we focus on the case $x = 0$. The transmission spectrum at $x = 0$ is shown in Fig. 3.9(a), where the origin of the detuning is taken to be the resonant frequency of the antisymmetric mode.

The mode splitting is seen to be $\delta\nu_{SA} = 54.16 \pm 0.22$ MHz, and the resonance associated with the antisymmetric mode is somewhat stronger and narrower than that associated with the symmetric mode. From the mode splitting we can infer the membrane transmission. Within our model, the mode splitting is independent of scattering losses and is given by

$$\delta\nu_{SA} = \frac{\Delta\nu}{\pi}\tan^{-1}\left(\frac{2\zeta_R}{\zeta_R^2-1}\left(1-\frac{\zeta_I^2}{\zeta_R^2-1}\right)\right) \tag{3.6}$$

$$\approx \frac{2}{\pi}(\sin^{-1}|t_m|)\Delta\nu, \tag{3.7}$$

where the last line results from making the approximation of a membrane without absorption loss, $\zeta_I \to 0$. This result agrees with that found in earlier work [32,64,65]. From Eq. (3.7) we infer $T_m = (8.07\pm0.06)\times10^{-4}$, with a corresponding polarizability of $\zeta_R = 35.18\pm0.14$. The correction to ζ_R induced by taking ζ_I to be 0 (as determined from the subsequent lineshape analysis) in Eq. (3.6) is negligible.

We next consider the lineshapes of the transmission resonances shown in Fig. 3.9(a). The transmission spectrum of the antisymmetric mode is found to be Lorentzian with FWHM and peak height given by

$$\frac{\kappa^{asym}}{2\pi} = \frac{S+T}{\pi}\Delta\nu \tag{3.8}$$

$$T_{peak}^{asym} = \frac{T^2}{\left(\left(1+\frac{(T+S)^2}{16}\zeta_R^2\right)+\frac{T+S}{2}\zeta_I\right)(T+S)^2}, \tag{3.9}$$

where $S = S_{diel} + S_m$. The expression for the linewidth is the same as (3.5) for the empty cavity, with the scattering losses now taken to be the sum of those for the membrane and the dielectric mirrors.

The FWHM and peak height of the symmetric mode are given by

$$\frac{\kappa^{sym}}{2\pi} = \frac{1}{\pi}\sqrt{\frac{(S+T)(8\zeta_I+(S+T)(1+\zeta_R^2))}{1+\zeta_R^2}}\Delta\nu \tag{3.10}$$

$$T_{peak}^{sym} = \frac{T^2}{(\frac{T+S}{2})^2+\left(\pi\frac{\delta\nu_{SA}}{\Delta\nu}\right)^2} \times\frac{1}{2\zeta_I(S+T)+(1+\zeta_R^2)\left(\frac{T+S}{2}\right)^2}, \tag{3.11}$$

where it has been assumed that $\zeta_R \gg 1$ (which is the case of interest). If $\zeta_I \neq 0$ the peak is not exactly Lorentzian, and it shows additional broadening due to absorption.

Taking the mirror properties T and S_{diel}, the fraction ϵ of power coupled into the TEM_{00} mode from the measurements of the empty cavity, and $\delta\nu_{SA}$ and ζ_R from the measured frequency splitting between the symmetric and antisymmetric modes (3.7), the only remaining parameters to be determined are the membrane scattering S_m and the imaginary part of the polarizability ζ_I. Fitting the transmission data, as shown in Fig. 3.9(a), to the equations from which (3.8)-(3.11) were derived yields $\zeta_I = 0.151 \pm 0.008$ and $S_m = (8.1 \pm 1) \times 10^{-4}$. These parameters may then be substituted into expressions for the cavity reflection based on the matrix model, and the results are overlaid on the reflection data in Fig. 3.9(b); the excellent agreement is a testament that our model accurately captures the underlying physics.

We now summarize the optical properties of the HCG as determined from our measurements. Within our model, the reflection and transmission of the slab parametrized by polarizability ζ are $|r'_m|^2 = |i\zeta/(1-i\zeta)|^2 = 0.99895 \pm 2 \times 10^{-5}$ and $|t'_m|^2 = |1/(1-i\zeta)|^2 = (8.07 \pm 0.06) \times 10^{-4}$. The corresponding absorption, appropriate for light incident from one side of the HCG, is $A_m = 1 - |r'_m|^2 - |t'_m|^2 = (2.34 \pm 0.28) \times 10^{-4}$. The transmission is thus approximately a factor of 3.5 higher

than the absorption. Scattering reduces the transmission and reflection by a factor e^{-S_m}, yielding $R_m = |r'_m|^2 e^{-S_m} = 0.9981$ and $T_m = |t'_m|^2 e^{-S_m} = 8.06 \times 10^{-4}$.

3.7 Conclusion

By using a membrane patterned as a subwavelength diffraction grating, we have implemented a "membrane in the middle" system with a membrane of very high reflectivity. The resonance spectrum is qualitatively different from those demonstrated to date using low-reflectivity membranes; rather than a sinusoidal modulation of frequency with membrane displacement, the spectrum is that of two cavities coupled by photon tunneling through a shared highly-reflecting mirror. The weak optical coupling manifests itself as an avoided crossing at the point where the left- and right-hand cavities are simultaneously resonant, and from the size of the avoided crossing we are able to precisely determine the membrane transmission.

Analysis of the avoided crossing allows additional insight into the loss mechanisms present in the subwavelength grating. The upper branch of the avoided crossing is a spatially symmetric mode, having nonzero overlap with the membrane, whereas the lower branch is antisymmetric, having (in the limit of a membrane of vanishing thickness) no overlap. Consequently, the symmetric mode suffers greater loss from absorption, manifest in the form of a weaker resonance peak with a larger linewidth. Losses unrelated to material absorption are the same for both modes, so that by comparing the two resonance peaks with those of the empty cavity, we are able to distinguish the effects of absorption and scattering. Furthermore,

straightforward modeling and more exhaustive experiments, involving injecting light from both sides of the cavity, could independently probe scattering losses from the two sides of the membrane.

The values found for the HCG properties agree reasonably well with those expected from RCWA calculations, although the measured absorption $A_m = 2.34 \times 10^{-4}$ is somewhat higher than the value $1.3 \times 10^{-4} < A < 1.5 \times 10^{-4}$ predicted by RCWA. Further reduction of absorption losses is possible by the use of stoichiometric Si_3N_4 [69] rather than the low-stress SiN that was used in this work. Scattering losses can in principle be reduced by further improving the fabrication process. The present study has concentrated exclusively on the optical properties of our "HCG in the middle" system. The HCG is, however, mechanically compliant, and future work will explore the optomechanical opportunities in this system.

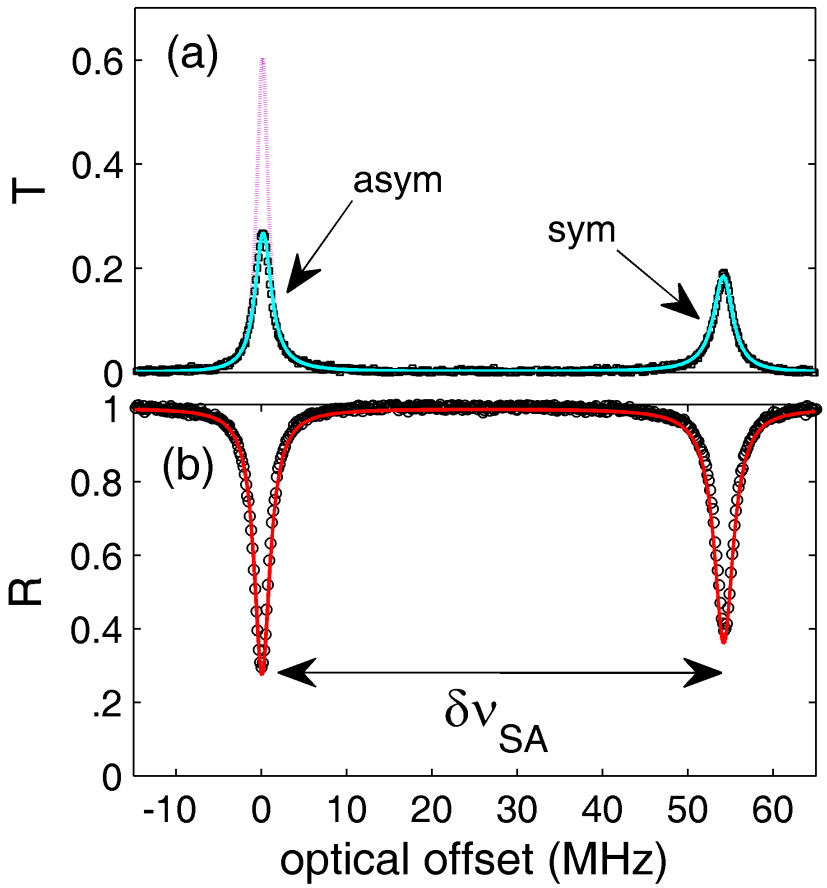

Fig. 3.9: (a) Transmission and (b) reflection at $x = 0$ (dashed line in Fig. 3.7). The two peaks correspond to the antisymmetric and symmetric modes. The taller peak (purple) in (a) is the empty cavity transmission. The overall reduction in height of both modes with respect to the empty cavity results from scattering losses, while the relatively smaller, broader peak of the symmetric mode results from absorption. The frequency separation $\delta\nu_{SA}$ is used to determine $|t_m|$ or ζ_R. The cyan curve superposed on the transmission data is a fit to our model, in which the only adjusted parameters are the loss terms S_m and ζ_I. The red curve superposed on the reflection data is not a fit, but rather the prediction of our model using the parameters S_m and ζ_I determined from the fit to the transmission data.

Chapter 4: Displacement sensing with mirror-in-the-middle cavity

4.1 Overview

One widely used methodology for displacement measurement is two-beam amplitude splitting interferometer [78], which requires calibration to determine the displacement from the electric output signal, and is susceptible to the noise in the reference arm. Another type of high resolution interferometer is the Fabry-Perot interferometer which is independent of an external reference arm.

Fabry-Perot interferometers are used to measure, e.g., small displacement inside tunneling microscope [80] and gravitational constant [81, 82]. An absolute uncertainty below 10 pm has been achieved by John Lawall [83]. Two methods were studied in Ref. [83]. One is the radio-frequency method, in which free spectral range is measured to give an absolute displacement measurement but lower resolution. The other is the optical method, which gives a much higher resolution but requires a reference laser.

Here we develop a technique for highly-sensitive displacement measurement. This technique is based on radio frequency measurement which can be measured with high accuracy. We are able to measure the displacement with a resolution of 4×10^{-14} m at a sampling rate of 10 Hz. This displacement sensing can be used to

analyze the stability and slow motion of the grating membrane in the mirror-in-the-middle cavity system.

4.2 Theory

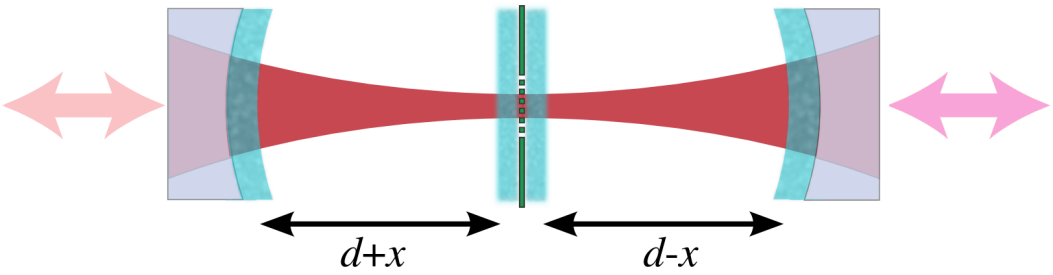

Fig. 4.1: Mirror-in-the-middle cavity.

Consider the mirror-in-the-middle cavity as shown in Fig. 4.1. We assume there is no the coupling between the two subcavities for simplicity. Similar to [83, 93, 94], the resonance conditions for the fundamental mode in the left and right cavity are given by

$$2\pi m_l = 2(2\pi \frac{f_l(x)}{c} - \Phi(d+x)) + \phi_l(f_l), \tag{4.1}$$

$$2\pi m_r = 2(2\pi \frac{f_r(x)}{c} - \Phi(d-x)) + \phi_r(f_r), \tag{4.2}$$

where f_l and f_r are the resonance frequencies of the left and right cavities, m_l and m_r are the mode numbers, $\phi_l(f_l)$ and $\phi_r(f_r)$ are the phase shifts at the mirrors, and $\Phi(d+x)$ and $\Phi(d-x)$ are the phase differences between a plane wave and a confined Gaussian beam. Specifically, $\Phi(d+x)$ and $\Phi(d-x)$ are

$$\Phi(d+x) = \sin^{-1}[\sqrt{(d+x)/R}], \tag{4.3}$$

$$\Phi(d-x) = \sin^{-1}[\sqrt{(d-x)/R}], \tag{4.4}$$

where R is the radius of the curved mirrors. For quarter-wave stack dielectric mirrors $\phi_l(f_l)$ and $\phi_r(f_r)$ are approximately linear in frequency,

$$\phi_l(f_l) = \phi_{l,0} + \alpha(f_l - f_{l,0}), \tag{4.5}$$

$$\phi_r(f_r) = \phi_{r,0} + \alpha(f_r - f_{r,0}), \tag{4.6}$$

where $\phi_{l,0}$ and $\phi_{r,0}$ are constants, and α is of the order of $1/f_0$. From the above equations, we have

$$2\pi m_l = 2(2\pi\frac{f_l(x)}{c} - \sin^{-1}[\sqrt{(d+x)/R}]) + \phi_{l,0} + \alpha(f_l - f_{l,0}), \tag{4.7}$$

$$2\pi m_r = 2(2\pi\frac{f_r(x)}{c} - \sin^{-1}[\sqrt{(d-x)/R}]) + \phi_{r,0} + \alpha(f_r - f_{r,0}), \tag{4.8}$$

Solving the above equations, we obtain

$$f_l(x) = \Delta f_l(x)(m_l + \frac{1}{\pi}\sin^{-1}\sqrt{\frac{d+x}{R}} - \frac{\phi_{l,0} - \alpha f_{l,0}}{2\pi}), \tag{4.9}$$

$$f_r(x) = \Delta f_r(x)(m_r + \frac{1}{\pi}\sin^{-1}\sqrt{\frac{d-x}{R}} - \frac{\phi_{r,0} - \alpha f_{r,0}}{2\pi}). \tag{4.10}$$

where $\Delta f_l(x) = \frac{1}{\frac{2(d+x)}{c} + \frac{\alpha}{2\pi}}$ and $\Delta f_r(x) = \frac{1}{\frac{2(d-x)}{c} + \frac{\alpha}{2\pi}}$ are the free spectral range of the left and right cavities. The difference between the resonance frequencies of the two

cavities is

$$\begin{aligned} F(x) &= f_r(x) - f_l(x) \\ &= \Delta f_r(x)(m_r + \frac{1}{\pi}\sin^{-1}\sqrt{\frac{d-x}{R}} - \frac{\phi_{r,0} - \alpha f_{r,0}}{2\pi}) \\ &\quad -\Delta f_l(x)(m_l + \frac{1}{\pi}\sin^{-1}\sqrt{\frac{d+x}{R}} - \frac{\phi_{l,0} - \alpha f_{l,0}}{2\pi}) \\ &= \frac{1}{\frac{1}{\Delta f_r(0)} - \frac{2x}{c}}(\frac{\sin^{-1}\sqrt{\frac{d-x}{R}} - \sin^{-1}\sqrt{\frac{d}{R}}}{\pi} + \frac{f_r(0)}{\Delta f_r(0)}) \\ &\quad -\frac{1}{\frac{1}{\Delta f_l(0)} + \frac{2x}{c}}(\frac{\sin^{-1}\sqrt{\frac{d+x}{R}} - \sin^{-1}\sqrt{\frac{d}{R}}}{\pi} + \frac{f_l(0)}{\Delta f_l(0)}). \end{aligned} \tag{4.11}$$

Given initial resonance frequency and free spectral range and geometry for each cavity (which are constants once fixed), we can obtain the position of the middle mirror by measuring the frequency difference between the two cavities. The response of the frequency difference to a variance δx in the position of the middle mirror is

$$\begin{aligned} \delta F(x) &= \frac{2(f_r(x)\Delta f_r(x) + f_l(x)\Delta f_l(x))}{c}\delta x \\ &\quad -\frac{1}{2\pi R}(\frac{\Delta f_r(x)}{\sqrt{\frac{d-x}{R}}\sqrt{1-\frac{d-x}{R}}} + \frac{\Delta f_l(x)}{\sqrt{\frac{d+x}{R}}\sqrt{1-\frac{d+x}{R}}})\delta x. \end{aligned} \tag{4.12}$$

When the middle mirror moves slightly away from the center ($\delta x \ll \lambda$ where λ is the wavelength of the laser), and neglecting the second term of Eq. 4.12 ($\sqrt{\frac{d-x}{R}}\sqrt{1-\frac{d-x}{R}}R \gg \lambda$, i.e. the cavity length is sufficiently away from the critical condition)

$$\delta F(x) \approx \frac{2(f_r(0)\Delta f_r(0) + f_l(0)\Delta f_l(0))}{c}\delta x. \tag{4.13}$$

Neglecting the second term in Eq. 4.12 results in an uncertainty of the order of $\frac{\lambda}{R}$. Noting that if the middle mirror is initially in the center, we have $f_l(0) =$

$f_r(0) = f_0 = 1/\lambda_0$ (choosing the same mode number for the two cavities) and $\Delta f_r(0) = \Delta f_l(0) = \Delta f_0$, we obtain

$$\frac{4\delta x}{\lambda_0} \approx \frac{\delta F(x)}{\Delta f_0}. \tag{4.14}$$

For small displacement ($\delta x \ll \lambda_0$), the uncertainty of the displacement measurement is dominated by the uncertainty of the frequency difference measurement, while the uncertainty due to the approximations made above is negligible. Otherwise we need to resort to Eq. 4.11

4.3 Experiment setup

The setup is quite similar to the one in Chapter 3, except that here we have two independent lasers injected from two sides. Here are the most relevant parameters. For the first part of the experiment we build an optical cavity with two high-reflectivity dielectric mirrors with nominal radii of curvature $R = 25$ mm. The cavity length is approximately 28 ± 6 μm below the stability boundary of $2R$. The confined mode thus has a waist (radius) of $\omega_0 = 17 \pm 1$ μm. This choice of waist here is for a compromise between minimizing beam spillage off of the patterned grating, and having a waist whose wavevectors have a narrow distribution of transverse momenta. We point out that for a general mirror-in-the-middle system, the choice of geometric parameters has a much wider range, as long as the two subcavities retain high quality factors throughout the measurement process when the middle mirror moves. Two independent lasers were aligned and locked to the cavity modes through Pound-Drever-Hall method, one from left and the other from the right side,

as shown in Fig. 4.1.

For the second part of the experiment we align the membrane (placed on a X-Y-Z stage with tip/tilt control) to the center of the optical cavity. It is adjusted to be normal to the cavity mode and located at the mode waist. The alignment is not so critical in this experiment compared to the one in the last chapter. The longitudinal location is confirmed by measuring the free spectral range of either subcavity, which shows that the membrane is within 2.3 μm of the center of the cavity. Each subcavity has one laser locked to its own optical mode.

4.4 Displacement sensing with the mirror-in-the-middle cavity

4.4.1 Empty cavity

This first experiment with the empty cavity is to show the resolution of our setup. It is generally not necessary for the displacement sensing in the mirror-in-the-middle system. The left laser is locked to one mode (m) of the empty cavity, and the right laser is locked to another mode ($m+1$) which is separated from the left laser by a free spectral range. Then we beat the two lasers and measure the beating frequency with a counter, and record the data for analysis. We show the power spectral density in Fig. 4.2, where we have converted the frequency to displacement using Eq. 4.14. The data was taken at a sampling rate of 1000 Hz for 8.192 s. We show the Allan deviation in Fig. 4.3. The noise floor is $\approx$0.6 kHz (or equivalently 4×10^{-14} m) at about 10 Hz. This measurement also tells us the free spectral range of the empty cavity, which is 2.993536 GHz with an uncertainty of 3 kHz. The

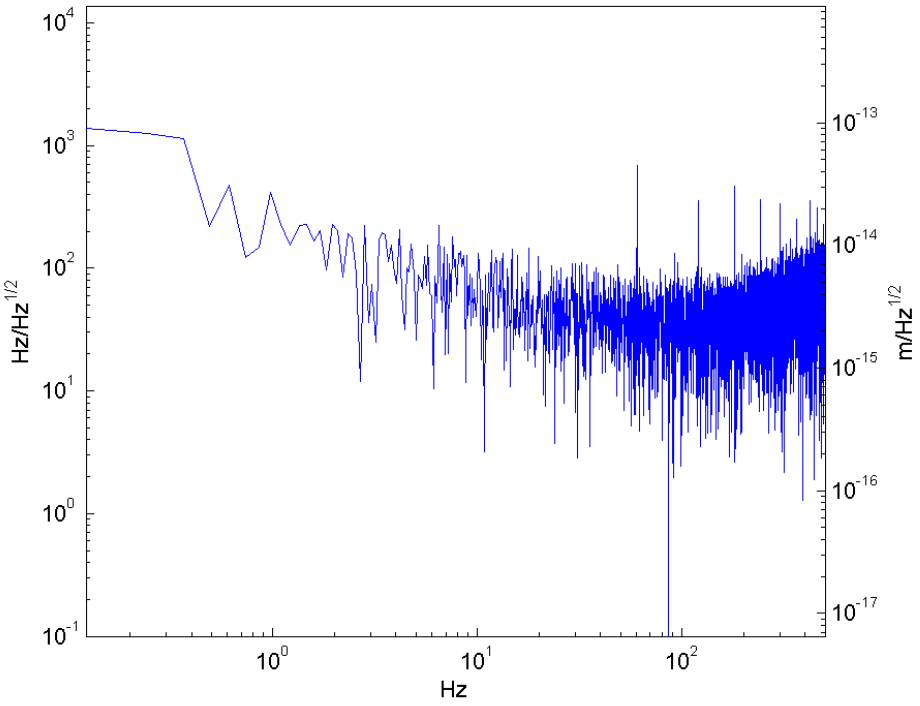

Fig. 4.2: Power spectral density of the frequency difference between the two lasers. The left laser is locked to one mode (m) of the empty cavity, and the right laser is locked to another mode ($m+1$) which is separated from the left laser by a free spectral range. The data was taken at a sampling rate of 1000 Hz for 8.192 s. The right axis is the conversion of frequency difference into distance.

noise comes mainly from the drift of the cavity and the Pound–Drever–Hall (PDH) locking technique. The drift of the cavity induces a change in the FSR. The noise in the PDH locking induces noise in the frequency of both lasers, which causes noise in the beating frequency.

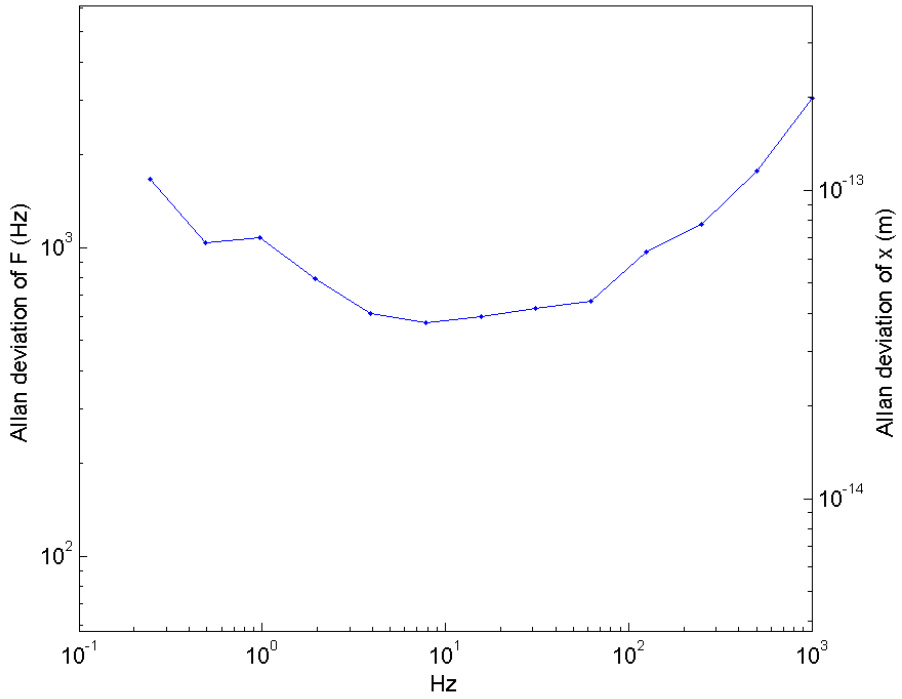

Fig. 4.3: Allan deviation of the frequency difference between the two lasers. The noise floor is ≈0.6 kHz (or equivalently 4×10^{-14} m) at about 10 Hz.

4.4.2 Mirror-in-the-middle cavity

Section 4.4.1 presented the characterization of the resolution and noise of our displacement sensing. In this section we apply this technique to measure the displacement of the middle mirror (in our case the membrane) to characterize the stability of the middle mirror. After aligning the middle mirror near to the center (avoid the anticrossing), we lock the left laser to the left cavity mode and the right laser to the right cavity mode. We choose the left cavity mode to be close to the right cavity mode, with a separation typically ranging from several hundred MHz to several GHz. Then we beat the two lasers and record the frequency difference with

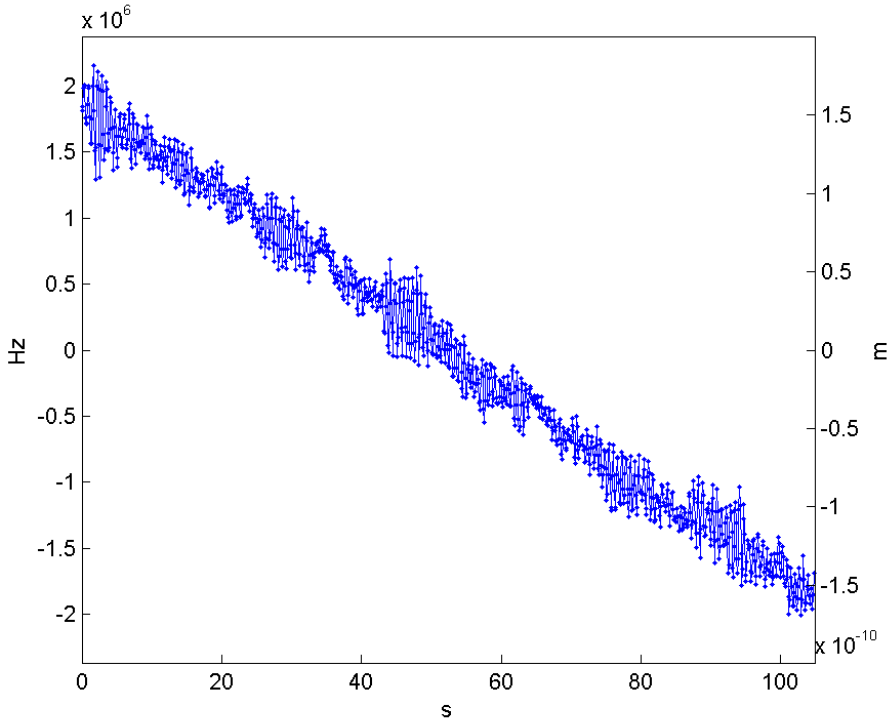

Fig. 4.4: Displacement measurement of the middle mirror. Data sampling rate is 10 Hz. The middle mirror is drifting at a rate of ≈ 3 pm/s.

a counter. Fig. 4.4 shows the data with a sampling rate of about 10 Hz. We notice a slow drift of the middle mirror at a rate of $\approx 3.05 \pm 0.03$ pm/s; the numeric value following the $\pm$ sign is the uncertainty given with a confidence level of 95%. The middle mirror is also oscillating at frequency of several Hz, confirmed by the power spectral density of the displacement shown in Fig. 4.5. The $1/f$ noise is mainly from the slow drift of the grating membrane, which is what we want to measure here.

Due to the small but nonzero transmission, the left and right cavity modes are coupled near the degeneracy point, where the resulting spectrum deviates from the linear spectrum and becomes insensitive to the displacement. We need to avoid the anticrossing for a displacement measurement. However, this is not a fundamental

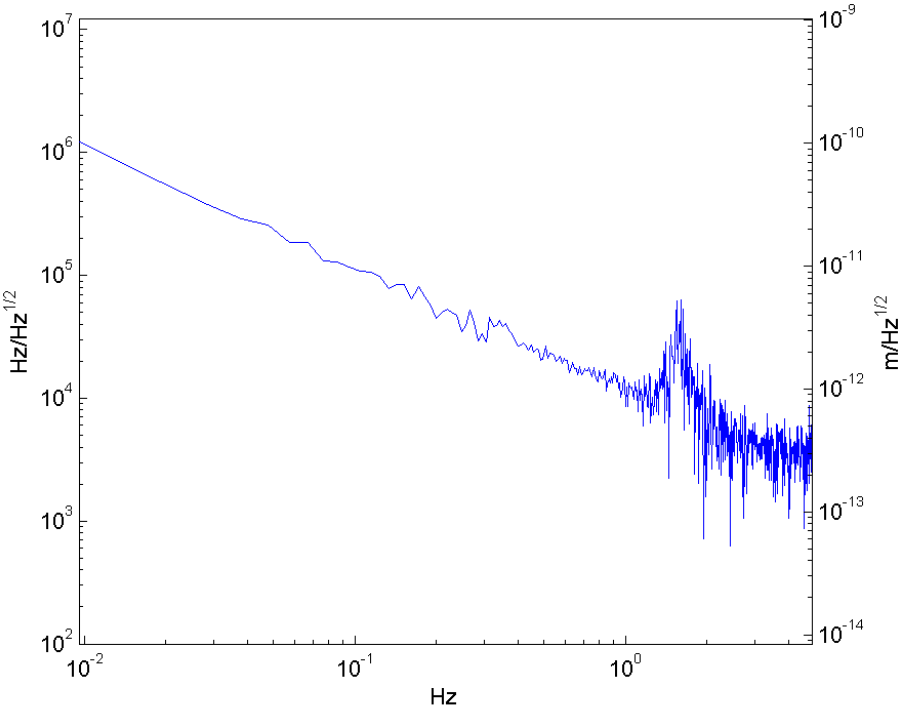

Fig. 4.5: Power spectral density of the displacement measurement. Data sampling rate is 10 Hz.

problem. For example, transmission can be eliminated by aligning the two cavities to different points on the middle mirror.

Chapter 5: Optomechanical interaction between light and a grating membrane

5.1 Overview

The radiation pressure force can change the dynamics of optomechanical systems. A stable optical trap for a gram-scale mirror has been reported, where the effective optical spring constant is orders of magnitude larger than the low frequency mechanical mode [86]. At larger light intensities when red detuned, the original equilibrium position becomes unstable and the effective optical spring potential may transit into a double well potential, which leads to optical bistability [87]. A Fabry-Perot interferometer filled with a medium whose refractive index depends on the light intensity can also be optically bistable [95]. Such bistable optical devices can be used as an optical switch, "transistor", and power limiter [95].

In this chapter we study theoretically two types of buckling transitions of the grating membrane in the mirror-in-the-middle system. The buckling transition can be observed using our displacement sensing technique developed in Chapter 4. The experiments will be pursued in our future research.

5.2 Buckling transition from radiation pressure

Consider the mirror-in-the-middle system same as in Chapter 4. The radiation pressure force comes from the momentum transfer when photons are reflected at the mirror. A single photon transfers a momentum of $2\hbar k$. The radiation pressure force is

$$\langle \hat{F} \rangle = 2\hbar k \frac{\langle \hat{a}^\dagger \hat{a} \rangle}{2L/c} = \hbar G \bar{n}, \tag{5.1}$$

where L is the length of the cavity, $G = \frac{\omega}{L}$ is the optomechanical coupling strength, and $\bar{n} = \langle \hat{a}^\dagger \hat{a} \rangle$ is the number of photons inside the cavity.

The number of photons inside the cavity can be obtained using the input-output formalism [96, 97] for the Fabry-Perot cavity. In the rotating frame, the evolution of the field operator $\hat{a}$ is described by the following equation of motion,

$$\dot{\hat{a}} = -i\Delta\hat{a} - \frac{\kappa}{2}\hat{a} + \sqrt{\kappa_{ex}}\hat{a}_{in} + \sqrt{\kappa_0}\hat{f}_{in}. \tag{5.2}$$

Here $\Delta = \omega_c - \omega_l$ is the laser detuning. $\hat{f}_{in}$ is the noise. $\kappa = \kappa_{ex} + \kappa_0$ is the cavity decay rate, where κ_{ex} is due to the input coupling, and κ_0 is due to other loss channels, such as scattering loss on the mirror. Take $\langle \hat{f}_{in} \rangle = 0$,

$$\langle \hat{a} \rangle = \frac{\sqrt{\kappa_{ex}} \langle \hat{a}_{in} \rangle}{\frac{\kappa}{2} + i\Delta} \tag{5.3}$$

for the steady state. Correspondingly, the photon number circulating inside the cavity is

$$\bar{n} = |\frac{\sqrt{\kappa_{ex}} \langle \hat{a}_{in} \rangle}{\frac{\kappa}{2} + i\Delta}|^2 = \frac{\kappa_{ex}}{(\frac{\kappa}{2})^2 + \Delta^2} \frac{P_{in}}{\hbar\omega_l}, \tag{5.4}$$

where P_{in} is the input laser power.

In our mirror-in-the-middle system, two lasers are coupled into the cavity, one from left side and the other from the right side. The frequencies of the two lasers are chosen so that they are red-detuned from their own subcavity mode by an amount of Δ. Keeping the laser frequencies fixed, when the middle mirror moves a distance of x, the resonance frequency changes in both subcavities but in opposite direction, which results in a change of photon numbers and the radiation pressure force. Specifically, the total radiation pressure force on the middle mirror is

$$F(x) = \left(\frac{\kappa_{ex} P_{in,l}/L_l}{(\frac{\kappa}{2})^2 + (\Delta + G_l x)^2} - \frac{\kappa_{ex} P_{in,r}/L_r}{(\frac{\kappa}{2})^2 + (\Delta - G_r x)^2}\right). \tag{5.5}$$

For simplicity we assume that $P_{in,l} = P_{in,r} = P_{in}$, $L_l \approx L_r \approx L$, and $G_l \approx G_r \approx G$, which does not change the physics of the buckling transition. The simplified radiation pressure force is

$$F(x) = \frac{\kappa_{ex} P_{in}}{L}\left(\frac{1}{(\frac{\kappa}{2})^2 + (\Delta + Gx)^2} - \frac{1}{(\frac{\kappa}{2})^2 + (\Delta - Gx)^2}\right). \tag{5.6}$$

When $\kappa \gg \Omega_m$ (resonance frequency of the mechanical mode of the middle mirror), the radiation pressure force reacts instantaneously to the motion of the mirror. There is a potential associated with the radiation pressure force,

$$F(x) = -\frac{\partial V_{rad}(x)}{\partial x}. \tag{5.7}$$

In our system, the radiation pressure potential is

$$V_{rad}(x) = \frac{2\kappa_{ex} P_{in}}{LG\kappa}\left(\arctan\left(\frac{2(\Delta - Gx)}{\kappa}\right) + \arctan\left(\frac{2(\Delta + Gx)}{\kappa}\right)\right). \tag{5.8}$$

For red-detuning, this potential has a maximum at $x = 0$, and for blue-detuning, it has a minimum instead, as shown in Fig. 5.1. Including the mechanical harmonic

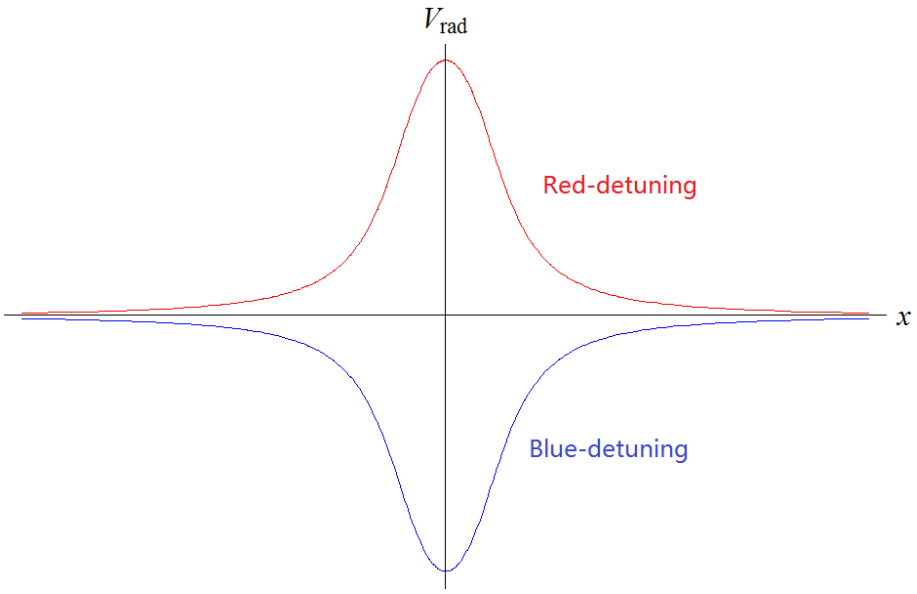

Fig. 5.1: Radiation pressure potential for red-detuning and blue-detuning.

potential, the overall potential becomes

$$V(x) = \frac{2\kappa_{ex}P_{in}}{LG\kappa}(\arctan(\frac{2(\Delta - Gx)}{\kappa}) + \arctan(\frac{2(\Delta + Gx)}{\kappa})) + \frac{m_{eff}\omega_m^2}{2}x^2. \quad (5.9)$$

The total spring constant is now

$$k = m_{eff}\omega_m^2 - \frac{32G\kappa_{ex}P_{in}}{L\kappa^4}(\frac{(-Gx+\Delta)}{\left(1+\frac{4(-Gx+\Delta)^2}{\kappa^2}\right)^2} + \frac{(Gx+\Delta)}{\left(1+\frac{4(Gx+\Delta)^2}{\kappa^2}\right)^2}). \quad (5.10)$$

From the above result, we can see that at $x = 0$, as we increase the red-detuned laser power P_{in}, the spring constant reduces to 0 and then becomes negative while two new local minimums build up in the potential, as shown in Fig. 5.2. On the other hand, when the laser is blue-detuned, the spring constant increases as the laser power increases, as shown in Fig. 5.3.

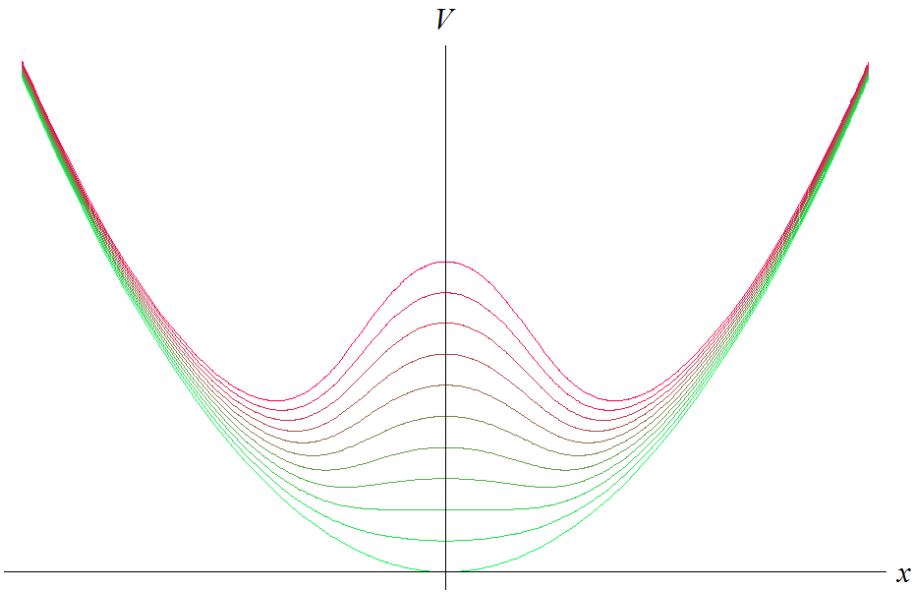

Fig. 5.2: Buckling transition of the mirror-in-the-middle system for red-detuned laser. From bottom to top, each line corresponds to an increase in the laser power by the same amount. The single well potential becomes double well potential as laser power increases.

5.3 Buckling transition from mode hybridization

In this section we study a buckling transition from mode hybridization, which leads to a power filter for the pump laser. Consider the same mirror-in-the-middle system, except that there is now only one laser, which is split by a 50/50 beam splitter and coupled into the cavity from both sides, as shown in Fig. 5.4. The Hamiltonian of the system is

$$\begin{aligned} H &= \Delta_L a_L^\dagger a_L + \Delta_R a_R^\dagger a_R - J(a_L^\dagger a_R + a_R^\dagger a_L) + Gx(a_L^\dagger a_L - a_R^\dagger a_R) \\ &\quad + \frac{p^2}{2m} + \frac{1}{2} m\omega_m^2 x^2. \end{aligned} \tag{5.11}$$

Here $\Delta_{L/R}$ is the detuning of the laser with regard to each subcavity, G is

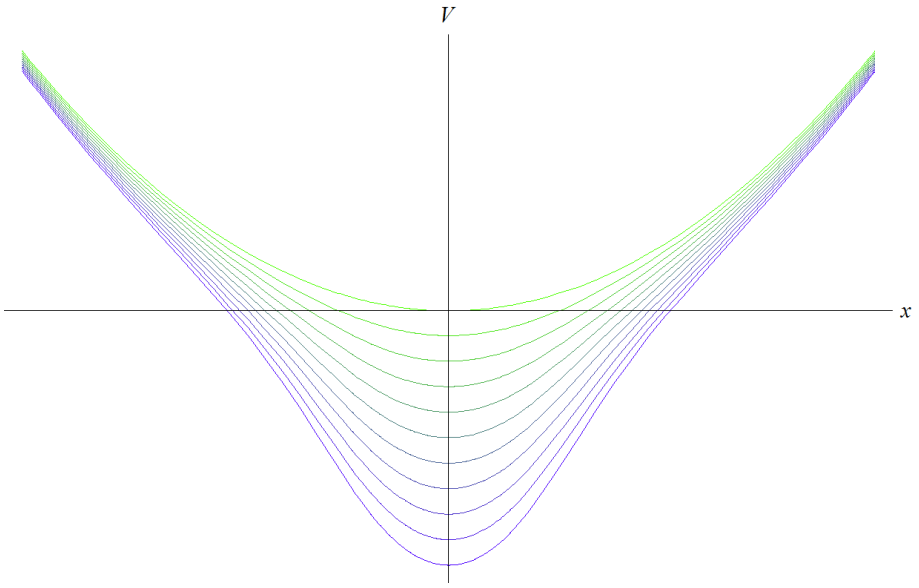

Fig. 5.3: Radiation pressure potential for blue-detuned laser. From top to bottom, each line corresponds to an increase in the laser power by the same amount. The spring constant increases as the laser power increases.

the optomechanical coupling parameter, J is the tunneling between the subcavities. Using the input-output formalism [96, 97], the equations of motion for the optical and mechanical degrees of freedom are as follows,

$$\dot{a}_L = -i\Delta_L a_L - iGxa_L + iJa_R - \frac{\kappa_L}{2}a_L + \sqrt{\kappa_L}a_{in,L} - i\sqrt{\kappa_L}\alpha_{in,L}, \quad (5.12)$$

$$\dot{a}_R = -i\Delta_R a_R + iGxa_R + iJa_L - \frac{\kappa_R}{2}a_R + \sqrt{\kappa_R}a_{in,R} - i\sqrt{\kappa_R}\alpha_{in,R}, \quad (5.13)$$

$$\dot{x} = \frac{p}{m}, \quad (5.14)$$

$$\dot{p} = -m\omega_m^2 x - \gamma p - G(a_L^\dagger a_L - a_R^\dagger a_R). \quad (5.15)$$

where $\kappa_{L/R}$ is the decay rate of each subcavity (assuming the only loss channel is the input coupling), $\alpha_{in,L/R}$ is the laser pump, $a_{in,L/R}$ is the vacuum fluctuation, and γ is the mechanical decay rate. Setting $x = 0$ to be at the avoided crossing,

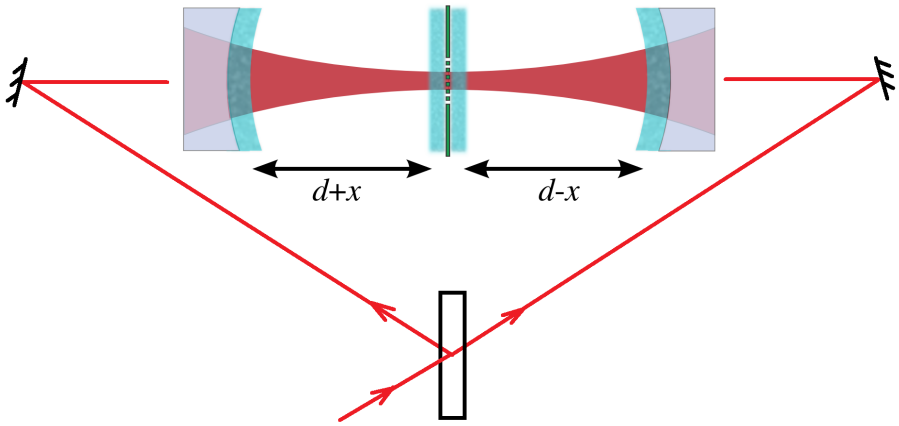

Fig. 5.4: Mirror-in-the-middle system. A laser is split by a beam splitter and coupled into the cavity from both sides.

where $\Delta_L = \Delta_R = \Delta$ and the eigenmodes are symmetric and antisymmetric. $a = \frac{1}{\sqrt{2}}(a_L + a_R)$ is the symmetric mode, and $b = \frac{1}{\sqrt{2}}(a_L - a_R)$ is the antisymmetric mode. Choosing $\kappa_L = \kappa_R = \kappa$, we have

$$\dot{a} = -(i\Delta_a + \frac{\kappa}{2})a - iGxb + \sqrt{\kappa}(a_{in} - i\alpha_{in}), \tag{5.16}$$

$$\dot{b} = -(i\Delta_b + \frac{\kappa}{2})b - iGxa + \sqrt{\kappa}(b_{in} - i\beta_{in}), \tag{5.17}$$

$$\dot{x} = \frac{p}{m}, \tag{5.18}$$

$$\dot{p} = -m\omega_m^2 x - \gamma p - G(a^\dagger b + b^\dagger a), \tag{5.19}$$

where$\Delta_a = \Delta - J$ is the detuning relative to the symmetric mode, and $\Delta_b = \Delta + J$ is the detuning to the antisymmetric mode. α_{in} and β_{in} are symmetric and antisymmetric parts of the laser pump. Here we focus on the case of symmetric pump where $\beta_{in} = 0$.

5.3.1 Steady state solution

We first find the steady state solution by applying a unitary transformation to the system such that: $a \to a + \alpha$, $b \to b + \beta$, $x \to x + X$. Taking a, b, a_{in}, b_{in}, x, and p to be 0, the Eqs. 5.16-5.19 become

$$0 = -(i\Delta_a + \frac{\kappa}{2})\alpha - iGX\beta - \sqrt{\kappa}i\alpha_{in}, \tag{5.20}$$

$$0 = -(i\Delta_b + \frac{\kappa}{2})\beta - iGX\alpha, \tag{5.21}$$

$$0 = -m\omega_m^2 X - G(\alpha^*\beta + \beta^*\alpha). \tag{5.22}$$

One solution is

$$\beta = X = 0, \tag{5.23}$$

$$\alpha = \frac{\sqrt{\kappa}\alpha_{in}}{-\Delta_a + i\frac{\kappa}{2}}. \tag{5.24}$$

A more subtle steady state solution where $\beta \neq 0$ is obtained as follows. From Eq. 5.21,

$$\alpha = \frac{(-\Delta_b + i\frac{\kappa}{2})}{GX}\beta. \tag{5.25}$$

From Eq. 5.22,

$$GX = -\frac{G^2}{m\omega_m^2}(\alpha^*\beta + \alpha\beta^*). \tag{5.26}$$

Inserting Eq. 5.25 into Eq. 5.26, we obtain

$$|\alpha|^2 = \frac{(\Delta_b^2 + \kappa^2/4)}{2\Delta_b}\frac{m\omega_m^2}{G^2}, \tag{5.27}$$

$$|\beta|^2 = \frac{m\omega_m^2}{2\Delta_b}X^2. \tag{5.28}$$

It turns out the symmetric part of light intensity inside the cavity is independent of the input laser power, while the antisymmetric part induces a shift of steady state position X of the middle mirror.

The stability of the solutions depends on the input laser power. For low power, the trivial solution is stable, while at high power, the nontrivial solution is stable just as happens in the laser transition. From Eq. 5.16 and Eq. 5.17,

$$\beta = \frac{-\sqrt{\kappa}\alpha_{in}GX}{(GX)^2 + \frac{\kappa^2}{4} - \Delta_a\Delta_b + i\frac{\kappa}{2}(\Delta_a + \Delta_b)} = |\beta|e^{i\phi}, \tag{5.29}$$

where $\phi = \tan^{-1}(\frac{-\frac{\kappa}{2}(\Delta_a+\Delta_b)}{(GX)^2+\frac{\kappa^2}{4}-\Delta_a\Delta_b})$ up to a constant π depending on the sign of X. Inserted into Eq. 5.28, we obtain

$$|\alpha_{in}| = \frac{|(gX)^2 + \frac{\kappa^2}{4} - \Delta_a\Delta_b + i\frac{\kappa}{2}(\Delta_a + \Delta_b)|}{G}\sqrt{\frac{m\omega_m^2}{2\kappa\Delta_b}}. \tag{5.30}$$

5.3.2 Buckling transition

Now we develop a model for the system near the instability. The Hamiltonian of the system after linearization is [41]

$$H = \Delta_a a^\dagger a + \Delta_b b^\dagger b + \omega_m c^\dagger c - g_0(c + c^\dagger)(b + b^\dagger) - G_0(c + c^\dagger)(a^\dagger b + b^\dagger a), \tag{5.31}$$

where $g_0 = G_0\alpha$ is the pump enhanced coupling. The last term is a nonlinear coupling. We require that $\omega_m \ll \Delta_b$, so that the polariton modes are close to the original uncoupled modes. First consider the linear Hamiltonian

$$H_{bc} = \Delta_b b^\dagger b + \omega_m c^\dagger c - g_0(c + c^\dagger)(b + b^\dagger). \tag{5.32}$$

Define

$$X_b = \frac{1}{\sqrt{2}}(b + b^\dagger), \tag{5.33}$$

$$P_b = \frac{1}{i\sqrt{2}}(b - b^\dagger), \tag{5.34}$$

$$X_c = \frac{1}{\sqrt{2}}(c + c^\dagger), \tag{5.35}$$

$$P_c = \frac{1}{i\sqrt{2}}(c - c^\dagger). \tag{5.36}$$

H_{bc} becomes

$$H_{bc} = \frac{1}{2}\Delta_b(X_b^2 + P_b^2) + \frac{1}{2}\omega_m(X_c^2 + P_c^2) - 2g_0 X_b X_c. \tag{5.37}$$

The above Hamiltonian can be diagonalized easily by the transformation

$$\begin{pmatrix} X_b \\ X_c \end{pmatrix} = \begin{pmatrix} u\sqrt{\frac{\Delta_b}{\omega_m}} & v\sqrt{\frac{\Delta_b}{\omega_m}} \\ -v & u \end{pmatrix} \begin{pmatrix} X_+ \\ X_- \end{pmatrix}, \tag{5.38}$$

$$\begin{pmatrix} P_b \\ P_c \end{pmatrix} = \begin{pmatrix} u\sqrt{\frac{\omega_m}{\Delta_b}} & v\sqrt{\frac{\omega_m}{\Delta_b}} \\ -v & u \end{pmatrix} \begin{pmatrix} P_+ \\ P_- \end{pmatrix}, \tag{5.39}$$

where u and v satisfy $u^2 + v^2 = 1$ and $2g_0(v^2 - u^2)\sqrt{\frac{\Delta_b}{\omega_m}} + uv(\Delta_b^2 - \omega_m^2) = 0$. Noting that $\omega_m \ll \Delta_b$, the resulting lower frequency branch Hamiltonian is

$$H_- = \frac{1}{2}\omega_m P_-^2 + \frac{1}{2}\omega_m(1 - \frac{4g_0^2}{\Delta_b\omega_m})X_-^2, \tag{5.40}$$

which is mainly the mechanical mode. As $\frac{4g_0^2}{\Delta_b\omega_m} \to 1$ with increasing pump power, this Hamiltonian goes unstable. Near the instability, the nonlinear term $V_{nl} = -G_0(c + c^\dagger)(a^\dagger b + b^\dagger a) = -Gx(a^\dagger b + b^\dagger a)$ becomes

$$V_{nl} = -G\sqrt{\frac{\omega_m}{\Delta_b}}(a + a^\dagger)X_-^2. \tag{5.41}$$

After another transformation by $e^{-AX_-^2(a-a^\dagger)}$ with $A = -\frac{G}{\Delta_a}\sqrt{\frac{\omega_m}{\Delta_b}}$, such as $e^{-Ax^2\left(a-a^\dagger\right)}ae^{Ax^2\left(a-a^\dagger\right)} = a - Ax^2$, we obtain an effective Hamiltonian

$$H_{eff} = \frac{1}{2}\omega_m(P_- - 2iA(a-a^\dagger)X_-)^2 + \frac{1}{2}\omega_m(1-\frac{4g_0^2}{\Delta_b\omega_m})X_-^2 + \Delta_a a^\dagger a - \Delta_a A^2 X_-^4. \quad (5.42)$$

We see that for $\Delta_a < 0$, the quadratic confinement at $X_- = 0$ changes to an inverted oscillator with a quartic wall. As the spring constant goes to 0, the system buckles into one of the two solutions of the double-well potential induced by coupling to the cavity mode a.

5.4 Conclusion

In this chapter we studied two types of buckling transitions in the mirror-in-the-middle system. The buckling transition arises fundamentally from the optomechanical interaction between laser and mechanical oscillator. The displacement sensing developed in Chapter 4 can be used to observe such phenomena. The buckling transition can be used to modify the effective potential of the mechanical oscillator. Interestingly, the nontrivial steady state behaves as a power filter, in which case the photon population in the symmetric mode is independent of the pump power.

APPENDIX

Chapter A: Fabrication of the Ring Resonator

This section is my fabrication procedure for the micro-ring resonator in the clean room of CNST at NIST. We start from a Silicon-On-Insulator (SOI) wafer. The thickness of the top silicon layer (which is the device layer) is 220 nm, and that of the silicon dioxide layer is 3 μm.

We first clean the wafer,

1. H_2O:NH_4OH:H_2O_2=5:1:1 bath at 80°C for 10 minutes.
2. Rinse in deionized (DI) water.
3. H_2O:HCL:H_2O_2=5:1:1 solution at 80°C for 10 min.
4. Rinse in DI water.
5. Blow dry the wafers.

After cleaning, we spin coat the wafer with electron beam resist (such as ZEP-520 or PMMA). Here we use ZEP-520 as an example.

1. Clean the chuck that holds the wafer and check the vacuum of the spinner.
2. Slowly add the resist onto the wafer with a pipette and avoid bubbles.

3. Spin wafer at 500 rpm for 5 seconds.

4. Spin wafer at 3000 rpm for 60 seconds.

5. Bake wafer at 180°C for 2 minutes.

Then we pattern the resist with electron beam lithography. As the JEOL tool is located in a different room other than the clean room, seal the wafer box when transporting the wafer between the rooms and avoid contamination from the dust in the air.

1. Load the wafer into the chamber.

2. Transfer the pattern gds file to the control computer and convert gds file to binary file. Change field size to 62.5 μm, and change the output unit to 8000. Check the pattern.

3. Edit a jdf file and a sdf file, and compile them to obtain a job file. Check the array.

4. Set the tool parameters. The accelerating voltage is set to be 100 keV, the aperture is 25 μm, and the current is 200 pA.

5. Run the calibration process.

6. Expose the wafer. The dose is 500 C/cm^2.

7. Unload the wafer.

Then we develop the pattern in a wet bench. Gently stir the solution during the development.

1. Dip the wafer in hexyl acetate 99% solution for 1 minute.

2. IPA rinse for 30 seconds.

3. Blow dry the wafer.

We continue to transfer the ring resonator pattern to the device layer with plasma etching. There are various recipes for silicon etching. Here we use HBr as an example.

1. Load the wafer into the chamber.

2. Wait for 2 minutes for temperature stabilization.

3. Set HBr flow to 100 sccm and H_2 flow to 2 sccm. RF forward power is 100W.

4. Etch the wafer for 7 minutes.

5. Unload the wafer.

Then we strip off the resist by Nanostrip and Piranha.

1. Dip wafer in Nanostrip for 30 minutes at 80°C.

2. Rinse the wafer in water.

3. Dip wafer in Piranha (H_2SO_4:H_2O_2=3:1) for 30 minutes.

4. Rinse and blow dry the wafer.

Now we have fabricated the ring resonator in the device layer, we go on to finish the pigtail structure for coupling laser into and out of the device. First we deposit a layer of SiO_2 on top of the wafer as the cladding layer.

1. Load the wafer into the low temperature oxide (LTO) furnace. Use the same slots for the device wafer and the dummy wafers to keep the deposit rate consistent each time.
2. Deposit for 1 hour and 30 minutes.
3. Unload the wafer. Cool down the wafer before putting into the wafer box.

Next we make the mask for use in photolithography.

1. Convert the pattern gds file to a job file.
2. Load the mask and check the vacuum.
3. Center and focus calibration.
4. Expose the mask.
5. Unload the mask and develop in the AZ 400K developer (1:3) for 60 seconds. Gently stir the developer.
6. Rinse in DI water and blow dry the mask.
7. Cr etching for 60 seconds.
8. Rinse in DI water.
9. Dip in PG remover at 70°C for 5 minutes.
10. Rinse in DI water.
11. Dip in Nanostrip for 2 minutes.

12. Rinse in DI water and dry the wafer with the dryer.

Then we perform the photolithography.

1. Bake the wafer at 190°C for 2 minutes.
2. Spin coat the wafer with LOR-3A at 3000 rpm for 35 seconds.
3. Bake at 190°C for 5 minutes.
4. Spin coat the wafer with S1813 at 4000 rpm for 45 seconds.
5. Bake at 115°C for 1 minute.
6. Load the wafer into the photolithography tool.
7. Align the pigtail pattern to the device layer.
8. Expose the mask for 5 seconds at 21 W with MA8.
9. Unload the wafer and develop in M319 for 60 seconds.

After the pattern is transferred to the photoresist, we coat the wafer with a metal layer using electron beam evaporation.

1. Load the wafer into the chamber and wait for the pressure to drop down to 3×10^{-6} torr.
2. Deposit 5 nm Cr at 0.5 Å/s.
3. Deposit 150 nm Ni at 1 Å/s.
4. Unload the wafer.

Then we do the lift-off process.

1. Dip in 1165 resist remover at 70°C for 10 minutes. Stir the solution during the lift-off.

2. Rinse with IPA and blow dry the wafer.

Now we are ready to transfer the final pattern to the SiO_2 layers with plasma etching .

1. Load into the chamber and wait for 2 minutes for temperature stabilization.

2. Etch the wafer for 1 hour. The RF forward power is 30 W. The C_4F_8 flow rate is 40 sccm, and O_2 flow rate is 26 sccm.

3. Unload the wafer.

Then we release the pigtail from the silicon with KOH solution and cleave the wafer to obtain appropriate size for optical measurement.

Chapter B: High-Contrast-Grating-Membrane Fabrication

Here we describe the procedure used for fabricating the silicon nitride membrane gratings.

First we clean the double side polished silicon wafers:

1. H_2O:NH_4OH:H_2O_2=5:1:1 bath at 80°C for 10 min.
2. Rinse in DI water.
3. 2% HF solution for 10 s.
4. Rinse bath.
5. H_2O:HCl:H_2O_2 5:1:1 solution at 80°C for 10 min.
6. Rinse in DI water.
7. Dry the wafers.

The cleaning process should be done right before the silicon nitride deposition. The deposition rate and uniformity depends strongly on how the wafers and the baffles are positioned in the furnace. Typically, 4" wafers are positioned with the following order:

- Position 2: 4" baffle.

- Position 14: 4” sample wafer.
- Position 26: 4” sample wafer.
- Position 38: 4” baffle.

The main/device surface should face outside. Next we spin coat the wafer with photoresist:

1. Bake the wafer at 115°C for 1 min.
2. Spin HMDS on the front side of the wafer.
3. Spin S1813 for 1 min. at 3000 rpm.
4. Bake the wafer at 115°C for 1 min.
5. Spin HMDS on the back side of the wafer.
6. Spin S1813 for 1 min. at 3000 rpm.
7. Bake the wafer at 115°C for 1 min.

Always use clean wafer tweezers and handle the wafer from the marker side. Before starting the procedure, it is very important to clean up the chuck to be used and the hot plate. After the baking steps, make sure the wafer cools down before spinning resist. Add a 5 s to 10 s low speed spin (500 rpm) before going to full spin speed. Monitor if the resist will cover the whole surface after the spin. Towards the end of the slow spin, if uncoated areas are visible, stop the spin procedure and put drops of resist on uncovered areas. Avoid moving the wafer horizontally on a surface, as

much as possible, in order to make sure that the photoresist or the nitride is not scratched.

After spin coating, expose the bottom side mask with the membrane patterns for 7.5 s with the MA6 (40 mW/cm^2). Then continue to plasma etching and place a small piece of dummy wafer underneath the wafer so that the wafer does not slide to the side of the chamber during the initial pumping:

1. O_2 at 14 sccm, 600 mTorr, 100 W RF power, for 10 s.

2. CHF_3 at 20 sccm, 4 mTorr, 200 W RF power, for 15 min.

Remove the photoresist by PG remover and Nanostrip:

1. PG remover at 70°C for 10 min.

2. Rinse in DI water.

3. Nanostrip at room temperature for 10 min.

4. Rinse in DI water.

5. Blow dry.

Do another round of photolithography and resist stripping, with two differences: i) During the exposure, do back side alignment using the top surface mask. ii) During dry etch do the CHF_3 step only for 5 min. Then continue with standard KOH etch procedure to etch away the silicon under the membrane. Make sure to use the ultrasound. Otherwise the bath temperature can be nonuniform. If the ultrasound

is harmful to the sample, heat up the bath with ultrasound and turn it off during the etch. Etch for 1.5 h.

After the KOH etch, spin coat the wafer with PMMA,

1. Bake the wafer at 180°C for 1 min.
2. Spin PMMA 950k A8 for 1 min. at 3500 rpm.
3. Bake the wafer at 180°C for 1 min.

Then use the Zeiss SEM/FIB tool to do the electron beam lithography. Use 30 kV accelerating voltage and a dose of 350 C/cm^2 for writing. After another plasma etching and resist stripping, dry the sample with critical point dryer. We show in Fig. 3.1 a sample we fabricated.

List of Publications

This thesis is partially based on the following publications:

1. Corey Stambaugh, **Haitan Xu**, Utku Kemiktarak, Jacob Taylor, and John Lawall, "From membrane-in-the-middle to mirror-in-the-middle with a high-reflectivity sub-wavelength grating", Ann. Phys.. doi: 10.1002/andp.201400142.

2. **Haitan Xu**, Mohammad Hafezi, J. Fan, J. M. Taylor, G. F. Strouse, and Zeeshan Ahmed, "Ultra-sensitive chip-based photonic temperature sensor using ring resonator structures", *Optics Express* 22, 3098 (2014).

3. Utku Kemiktarak, Corey Stambaugh, **Haitan Xu**, Jacob Taylor, John Lawall, "Optomechanics with high-contrast gratings", *Proc. SPIE* 8995, High Contrast Metastructures III, 89950P (2014).

Other publications produced during my thesis work include:

1. **Haitan Xu** and J. M. Taylor, "Unified approach to topological quantum computation with anyons: From qubit encoding to Toffoli gate", *Physical Review A* 84, 012332 (2011)

2. **Haitan Xu** and J. M. Taylor, "Developing a robust approach to implementing non-Abelian anyons and topological quantum computing in a modified Kitaev honeycomb lattice model", arXiv:1104.0024.

3. V. Srinivasa, **H. Xu** and J. M. Taylor, "Tunable spin qubit coupling mediated by a multi-electron quantum dot", arXiv:1312.1711.

Bibliography

[1] Y. X. Woo, Z. K. Nagy, R. B. H. Tan, and R. D. Braatz, "Adaptive concentration control of cooling and antisolvent crystalllization with laser backscattering measurement," Cryst. Growth Des. 9, 182–191 (2009).

[2] M. R. Pinsky, L. Brochard, J. Mancebo, and G. Hedenstierna, eds., Applied Physiology in Intensive Care Medicine (Springer, 2009).

[3] K. R. A. Wunderlich, On the Temperature in Diseases: A Manual of Medical Thermometry (The New Sydenham Society, 1868), Vol. XLIX.

[4] F. A. Jolesz, "MRI-guided focused ultrasound surgery," Annu. Rev. Med. 60(1), 417–430 (2009).

[5] H. W. Standford III, HVAC Water Chillers and Cooling Towers (CRC Press Taylor & Francis Group, 2012).

[6] J. Turner, ed., Automotive Sensor, Sensors Technology (Momentum Press LLC, 2009).

[7] R. Price, "The Platinum resistance Thermometer," Platin. Met. Rev. 3, 78–87 (1959).

[8] G. F. Strouse, "Standard Platinum Resistance Thermometer Calibrations from the Ar TP to the Ag FP", NIST Special Publication 250–250–81 (2008).

[9] S. J. Mihailov, "Fiber Bragg grating sensors for harsh environments," Sensors (Basel) 12(12), 1898–1918 (2012).

[10] A. D. Kersey and T. A. Berkoff, "Fiber-optic Bragg-grating differential-temperature sensor," Photonics Technology Letters, IEEE 4(10), 1183–1185 (1992).

[11] R. Yun-Jiang, D. J. Webb, D. A. Jackson, Z. Lin, and I. Bennion, "In-fiber Bragg-grating temperature sensor system for medical applications," Lightwave Technology, Journalism 15, 779–785 (1997).

[12] J. Hecht, Understanding Fiber Optics 4th ed. (Prentice Hall, 2002).

[13] D. A. Krohn, Fiber Optic Sensors: Fundamentals and Applications 3ed. (ISA, 2000).

[14] F. L. Walls and D. W. Allan, "Measurements of frequency stability," Proc. IEEE 74(1), 162–168 (1986).

[15] G. F. Strouse, "Sapphire whispering gallery thermometer," Int. J. Thermophys. 28(6), 1812–1821 (2007).

[16] W. W. Rigrod, "The optical ring resonator," Bell Syst. Tech. J. 44(5), 907–916 (1965).

[17] L. Stern, I. Goykhman, B. Desiatov, and U. Levy, "Frequency locked micro disk resonator for real time and precise monitoring of refractive index," Opt. Lett. 37(8), 1313–1315 (2012).

[18] X. Tu, J. Song, T.-Y. Liow, M. K. Park, J. Q. Yiying, J. S. Kee, M. Yu, and G.-Q. Lo, "Thermal independent Silicon-Nitride slot waveguide biosensor with high sensitivity," Opt. Express 20(3), 2640–2648 (2012).

[19] M.-S. Kwon and W. H. Steier, "micro-ring-resonator-based sensor measuring both the concentration and temperature of a solution," Opt. Express 16(13), 9372–9377 (2008).

[20] B. Guha, B. B. C. Kyotoku, and M. Lipson, "CMOS-compatible athermal silicon micro-ring resonators," Opt. Express 18(4), 3487–3493 (2010).

[21] B. Guha, K. Preston, and M. Lipson, "Athermal silicon micro-ring electro-optic modulator," Opt. Lett. 37(12), 2253–2255 (2012).

[22] G.-D. Kim, H.-S. Lee, C.-H. Park, S.-S. Lee, B. T. Lim, H. K. Bae, and W.-G. Lee, "Silicon photonic temperature sensor employing a ring resonator manufactured using a standard CMOS process," Opt. Express 18(21), 22215–22221 (2010).

[23] K. Tiefenthaler and W. Lukosz, "Integrated optical switches and gas sensors," Opt. Lett. 9(4), 137–139 (1984).

[24] K. Tiefenthaler and W. Lukosz, "Grating couplers as integrated optical humidity and gas sensors," Thin Solid Films 126(3-4), 205–211 (1985).

[25] L. D. Turner, K. P. Weber, C. J. Hawthorn, and R. E. Scholten, "Frequency noise characterisation of narrow linewidth diode lasers," Opt. Commun. 201(4-6), 391–397 (2002).

[26] M. L. Gorodetsky and I. S. Grudinin, "Fundamental thermal fluctuations in microspheres," J. Opt. Soc. Am. B 21(4), 697–705 (2004).

[27] M. Aspelmeyer, T. J. Kippenberg, and F. Marquardt, "Cavity Optomechanics", arxiv:1303.0733(March) (2013).

[28] A. D. O'Connell, M. Hofheinz, M. Ansmann, R. C. Bialczak, M. Lenander, E. Lucero, M. Neeley, D. Sank, H. Wang, M. Weides, J. Wenner, J. M. Martinis, and A. N. Cleland, "Quantum ground state and single-phonon control of a mechanical resonator", Nature 464(7289), 697–703 (2010).

[29] D. W. C. Brooks, T. Botter, S. Schreppler, T. P. Purdy, N. Brahms, and D. M. Stamper-Kurn, "Non-classical light generated by quantum-noise-driven cavity optomechanics", Nature 488(7412), 476–480 (2012).

[30] A. H. Safavi-Naeini, S. Groblacher, J. T. Hill, J. Chan, M. Aspelmeyer, and O. Painter, "Squeezed light from a silicon micromechanical resonator", Nature 500(7461), 185–189 (2013).

[31] T. P. Purdy, P. L. Yu, R. W. Peterson, N. S. Kampel, and C. A. Regal, "Strong Optomechanical Squeezing of Light ", Physical Review X 3, 031012 (2013).

[32] M. Bhattacharya, H. Uys, and P. Meystre, "Multiple membrane cavity optomechanics", Phys. Rev. A 78, 041801 (2008).

[33] J. D. Thompson, B. M. Zwickl, A. M. Jayich, F. Mar- quardt, S. M. Girvin, and J. G. E. Harris, "Strong dispersive coupling of a high-finesse cavity to a micromechanical membrane", Nature 452, 72–75 (2008).

[34] T. P. Purdy, R. W. Peterson, and C. A. Regal, "Observation of Radiation Pressure Shot Noise on a Macroscopic Object", Science 339, 801–804 (2013).

[35] M. Karuza, C. Biancofiore, M. Bawaj, C. Molinelli, M. Galassi, R. Natali, P. Tombesi, G. Di Giuseppe, and D. Vitali, "Optomechanically induced transparency in a membrane-in-the-middle setup at room temperature", Phys. Rev. A 88(1) (2013).

[36] A. B. Shkarin, N. E. Flowers-Jacobs, S. W. Hoch, A. D. Kashkanova, C. Deutsch, J. Reichel, and J. G. E. Harris, "Optically Mediated Hybridization between Two Mechanical Modes", Phys. Rev. Lett. 112, 013602 (2014).

[37] A. Xuereb, C. Genes, and A. Dantan, "Collectively enhanced optomechanical coupling in periodic arrays of scatterers", Phys. Rev. A 88, 053803 (2013).

[38] A. Xuereb, C. Genes, and A. Dantan, "Strong Coupling and Long-Range Collective Interactions in Optomechanical Arrays", Phys. Rev. Lett. 109, 223601 (2012).

[39] C. Genes, A. Xuereb, G. Pupillo, and A. Dantan, "Enhanced optomechanical readout using optical coalescence", Phys. Rev. A 88, 033855 (2013).

[40] X. Xu and J. M. Taylor, "Beating the standard quantum limit for force sensing with a coupled two-mode optomechanical system", arXiv:1303.7469 (2013).

[41] X. Xu, M. Gullans, and J. M. Taylor, "Quantum Nonlinear Optics Near Optomechanical Instabilities", arxiv:1404.3726 (2014).

[42] J. Sankey, C. Yang, B. Zwickl, A. Jayich, and J. Harris, "Strong and Tunable Nonlinear Optomechanical Coupling in a Low-loss System", Nat. Phys. 6, 707–712 (2010).

[43] N. E. Flowers-Jacobs, S. W. Hoch, J. C. Sankey, A. Kashkanova, A. M. Jayich, C. Deutsch, J. Reichel, and J. G. E. Harris, "Fiber-cavity-based optomechanical device", Appl. Phys. Lett. 101, 221109 (2012).

[44] A. Xuereb and P. Domokos, "Dynamical scattering models in optomechanics: going beyond the 'coupled cavities' model", New J. Phys. 14, 095027 (2012).

[45] P. Rabl, "Photon Blockade Effect in Optomechanical Systems", Phys. Rev. Lett. 107, 063601 (2011).

[46] P. Kómár, S. D. Bennett, K. Stannigel, S. J. M. Habraken, P. Rabl, P. Zoller, and M. D. Lukin, "Single-photon nonlinearities in two-mode optomechanics", Phys. Rev. A 87, 013839 (2013).

[47] M. Ludwig, A. H. Safavi-Naeini, O. Painter, and F. Marquardt, "Enhanced Quantum Nonlinearities in a Two-Mode Optomechanical System", Phys. Rev. Lett. 109, 063601 (2012).

[48] S. Fan and J. Joannopoulos, "Analysis of Guided Resonances in Photonic Crystal Slabs", Phys. Rev. B 65, 235112 (2002).

[49] T. Antoni, A. G. Kuhn, T. Briant, P. F. Cohadon, A. Heidmann, R. Braive, A. Beveratos, I. Abram, L. L. Gratiet, I. Sagnes, and I. Robert-Philip, "Deformable

two-dimensional photonic crystal slab for cavity optomechanics", Opt. Lett. 36, 3434–3436 (2011).

[50] T. Antoni, K. Makles, R. Braive, T. Briant, P. F. Cohadon, I. Sagnes, I. Robert-Philip, and A. Heidmann, "Nonlinear mechanics with suspended nanomembranes ", EPL 100, 68005 (2012).

[51] C. H. Bui, J. Zheng, S. W. Hoch, L. Y. T. Lee, J. G. E. Harris, and C. Wei Wong, "High-reflectivity, high-Q micromechanical membranes via guided resonances for enhanced optomechanical coupling", Appl. Phys. Lett. 100, 021110 (2012).

[52] M. C. Huang, Y. Zhou, and C. J. Chang-Hasnain, "A surface-emitting laser incorporating a high-index-contrast subwavelength grating", Nat Photon 1, 119–122 (2007).

[53] F. Brückner, D. Friedrich, T. Clausnitzer, M. Britzger, O. Burmeister, K. Danzmann, E. B. Kley, A. Tünnermann, and R. Schnabel, "Realization of a Monolithic High-Reflectivity Cavity Mirror from a Single Silicon Crystal", Phys. Rev. Lett. 104, 163903 (2010).

[54] F. Lu, F. G. Sedgwick, V. Karagodsky, C. Chase, and C. J. Chang-Hasnain, "Planar high-numerical-aperture low-loss focusing reflectors and lenses using subwavelength high contrast gratings", Opt. Express 18, 12606– 12614 (2010).

[55] D. Fattal, J. Li, Z. Peng, M. Fiorentino, and R. G. Beausoleil, "Flat dielectric grating reflectors with focusing abilities", Nat. Photonics 4, 466–470 (2010).

[56] C. J. Chang-Hasnain, Semicond. "High-contrast Gratings As a New Platform for Integrated Optoelectronics", Sci. Technol. 26, 014043 (2011).

[57] U. Kemiktarak, M. Metcalfe, M. Durand, and J. Lawall, "Mechanically compliant grating reflectors for optomechanics", Appl. Phys. Lett. 100, 061124 (2012).

[58] V. Karagodsky, F. G. Sedgwick, and C. J. Chang- Hasnain, "Theoretical analysis of subwavelength high contrast grating reflectors", Opt. Express 18, 16973–16988 (2010).

[59] M. Moharam and T. Gaylord, "Rigorous coupled-wave analysis of planar-grating diffraction", JOSA 71(7), 811–818 (1981).

[60] C. Stambaugh, M. Durand, U. Kemiktarak, and J. Lawall, "Cavity-enhanced measurements for determining dielectric-membrane thickness and complex index of refraction", Appl. Opt. 53, 4930–4938 (2014).

[61] U. Kemiktarak, M. Durand, M. Metcalfe, and J. Lawall, "Cavity optomechanics with sub-wavelength grating mirrors", New J. Phys. 14, 125010 (2012).

[62] G. Fowles, Introduction to Modern Optics, Dover Books on Physics Series (Dover Publications, 1975).

[63] M. B. Spencer and W. E. Lamb, "Theory of Two Coupled Lasers", Phys. Rev. A 5, 893–898 (1972).

[64] W. Fader, Quantum Electronics, IEEE Journal of 21(11), 1838–1844 (1985).

[65] W. W. Chow, Quantum Electronics, IEEE Journal of 22(8), 1174–1183 (1986).

[66] H. Kogelnik and T. Li, "Laser Beams and Resonators", Proc. IEEE 54, 1312–1329 (1966).

[67] C. Hood, H. J. Kimble, and J. Ye, "Characterization of high-finesse mirrors: Loss, phase shifts, and mode structure in an optical cavity", Phys. Rev. A 64, 033804 (2001).

[68] A. Siegman, Lasers, (University Science Books, Sausalito, 1986).

[69] D. Wilson, C. Regal, S. Papp, and H. Kimble, "Cavity Optomechanics with Stoichiometric SiN Films", Phys. Rev. Lett. 103, 207204 (2009).

[70] P. Giacomo, "News from the BIPM", Metrologia 20, 25-30 (1984).

[71] B. J. Bloom, T. L. Nicholson, J. R. Williams, S. L. Campbell, M. Bishof, X. Zhang, W. Zhang, S. L. Bromley, and J. Ye, "An optical lattice clock with accuracy and stability at the 10^{-18} level", Nature 506, 71–75 (2014).

[72] N. Hinkley, J. A. Sherman, N. B. Phillips, M. Schioppo, N. D. Lemke, K. Beloy, M. Pizzocaro, C. W. Oates, A. D. Ludlow, "An atomic clock with 10^{-18} instability", Science 341, 1215 (2013).

[73] A. Einstein, "Zur Elektrodynamik bewegter Körper", Annalen der Physik. 17 891 (1905).

[74] P. L. Bender, D. G. Currie, R. H. Dicke, D. H. Eckhardt, J. E. Faller, W. M. Kaula, J. D. Mulhollai H. H. Plotkin, S. K. Poultney, E. C. Silverberg, D. T. Wilkinson, J. G. Williams, and C. O. Alley, "The Lunar Laser Ranging Experiment", Science 182, 229 (1973).

[75] C. O. Alley, R. F. Chang, D. G. Curri, J. Mullendore, S. K. Poultney, J. D. Rayner, E. C. Silverberg, C. A. Steggerda, H. H. Plotkin, W. Williams, B. Warner, H. Richardson, and B. Bopp, "Apollo 11 Laser Ranging Retro-Reflector: Initial Measurements from the McDonald Observatory", Science 167, 368 (1970).

[76] C. O. Alley, R. F. Chang, D. G. Currie, S. K. Poultney, P. L. Bender, R. H. Dicke, D. T. Wilkinson, J. E. Faller, W. M. Kaula, G. J. F. MacDonald, J. D. Mulholland, H. H. Plotkin, W. Carrion, and E. J. Wampler, "Laser Ranging Retro-Reflector: Continuing Measurements and Expected Results", Science 167, 458 (1970).

[77] Christopher J. Hegarty and Eric Chatre, "Evolution of the Global Navigation SatelliteSystem (GNSS)", Proceedings of the IEEE 96, 1902 (2008).

[78] N Bobroff, "Recent advances in displacement measuring interferometry", Meas. Sci. Technol. 4, 907 (1993).

[79] A. Einstein, "Prinzipielles zur allgemeinen Relativitätstheorie", Annalen der Physik 55, 241 (1918).

[80] L. Howard, J. Stone, and J. Fu, "Real-time displacement measurements with a Fabry-Perot cavity and a diode laser," Precis. Eng. 25, 321 (2001).

[81] H. V. Parks, J. E. Faller, and D. S. Robertson, "A suspended laser interferometer for determining the Newtonian constant of gravitation," IEEE Trans. Instrum. Meas. 50, 598 (2001).

[82] W.-T. Ni, D.-K. Liu, T.-T. Liu, H.-H. Mei, S. Shi Pan, C.-P. Pang, and H.-C. Yeh, "The application of laser metrology and resonant optical cavity techniques to the measurement of G," Meas. Sci. Technol. 10, 495 (1999).

[83] John R. Lawall, "Fabry–Perot metrology for displacements up to 50 mm", JOSA A 22, 2786(2005).

[84] Osamu Miyakawa, Robert Ward, Rana Adhikari, Matthew Evans, Benjamin Abbott, Rolf Bork, Daniel Busby, Jay Heefner, Alexander Ivanov, Michael Smith, Robert Taylor, Stephen Vass, Alan Weinstein, Monica Varvella, Seiji Kawamura, Fumiko Kawazoe, Shihori Sakata, and Conor Mow-Lowry, "Measurement of optical response of a detuned resonant sideband extraction gravitational wave detector ", Phys. Rev. D 74, 022001 (2006).

[85] Alessandra Buonanno and Yanbei Chen, "Signal recycled laser-interferometer

gravitational-wave detectors as optical springs", Phys. Rev. D 65, 042001 (2002).

[86] Thomas Corbitt, Yanbei Chen, Edith Innerhofer, Helge Müller-Ebhardt, David Ottaway, Henning Rehbein, Daniel Sigg, Stanley Whitcomb, Christopher Wipf, and Nergis Mavalvala, "An All-Optical Trap for a Gram-Scale Mirror", Phys. Rev. Lett. 98, 150802 (2007).

[87] A. Dorsel, J. D. McCullen, P. Meystre, E. Vignes, and H. Walther , "Optical Bistability and Mirror Confinement Induced by Radiation Pressure", Phys. Rev. Lett. 51, 1550 (1983).

[88] Mohammad Hafezi, Eugene A. Demler, Mikhail D. Lukin, and Jacob M. Taylor, "Robust optical delay lines with topological protection", Nature Physics 7, 907 (2011).

[89] M. Hafezi, S. Mittal, J. Fan, A. Migdall, and J. M. Taylor, "Imaging topological edge states in silicon photonics", Nature Photonics 7, 1001 (2013).

[90] Mohammad Hafezi, Mikhail D Lukin, and Jacob M Taylor, "Non-equilibrium fractional quantum Hall state of light ", New J. Phys. 15 063001 (2013).

[91] Haitan Xu and J. M. Taylor, "Unified approach to topological quantum computation with anyons From qubit encoding to Toffoli gate", Phys. Rev. A 84, 012332 (2011).

[92] Haitan Xu and J. M. Taylor, "Developing a robust approach to implementing non-Abelian anyons and topological quantum computing in a modified Kitaev honeycomb lattice model", arXiv:1104.0024.

[93] Mathieu Durand, John Lawall, and Yicheng Wang, "High-accuracy Fabry–Perot displacement interferometry using fiber lasers", Meas. Sci. Technol. 22 094025 (2011)

[94] Mathieu Durand, Yicheng Wang, and John Lawall, "Accurate Gouy phase measurement in an astigmatic optical cavity", Appl. Phys. B 108, 749 (2012).

[95] J. H. Marburger and F. S. Felber, "Theory of a lossless nonlinear Fabry-Perot interferometer", Phys. Rev. A 17, 335 (1978).

[96] C. W. Gardiner and M. J. Collett, "Input and output in damped quantum systems Quantum stochastic differential equations and the master equation", Phys. Rev. A 31, 3761 (1985).

[97] C. W. Gardiner, and P. Zoller, Quantum Noise (Springer Series in Synergetics) (2004).

[98] Corey Stambaugh, Haitan Xu, Utku Kemiktarak, Jacob Taylor, and John Lawall, "From membrane-in-the-middle to mirror-in-the-middle with a high-reflectivity sub-wavelength grating", Ann. Phys.. doi: 10.1002/andp.201400142.

[99] Haitan Xu, Mohammad Hafezi, J. Fan, J. M. Taylor, G. F. Strouse, and Zeeshan Ahmed, "Ultra-sensitive chip-based photonic temperature sensor using ring resonator structures", Optics Express 22, 3098 (2014).

[100] Utku Kemiktarak, Corey Stambaugh, **Haitan Xu**, Jacob Taylor, John Lawall, "Optomechanics with high-contrast gratings", *Proc. SPIE* 8995, High Contrast Metastructures III, 89950P (2014).